CERN LIBRARIES, GENEVA

CM-P00045106

CERN BIBLIOTHEQUE repl. 13 6 88

SPS

CERN-SPSC/83-51
SPSC/P189
22 Aug. 1983

PROPOSAL TO THE SPSC

LEPTON PRODUCTION

H. Gordon, T. Ludlam, V.A. Polychronakos, D.C. Rahm, I. Stumer
Brookhaven National Laboratory

T. Åkesson, H. Atherton, H. Breuker, C.W. Fabjan, U. Goerlach, G. London*, L. Olsen, W.J. Willis
CERN

P. Glaessel, J. Schukraft, H.J. Specht
Heidelberg University

S. Mayburov, A. Shmeleva
Lebedev Institute, Moscow

V. Sidorov
Novosibirsk Institute of Nuclear Physics

S. Almehed, G. Jarlskog, B. Lörstad
Lund University

V. Cherniatin, B. Dolgoshein, Yu. Golubkov, A. Kalinovsky, V. Kantserov, P. Nevsky, A. Sumarakov
Moscow Physical Engineering Institute

N.A. McCubbin
Rutherford Appleton Laboratory

D. Bettoni, M. Goldberg, N. Horwitz, G.C. Moneti
Syracuse University

O. Benary, S. Dagan, D. Lissauer, Y. Oren
Tel Aviv University

ABSTRACT

This experiment aims to settle open questions in the production of electrons, muons, and neutrinos. Prominent among these are e/μ universality, anomalies in the production of single leptons, the contribution of charm decay to lepton pair (Drell-Yan) production, and the "anomalous" low mass pairs. The experimental design optimizes the combination of electron identification, muon identification, missing energy measurement (for neutrinos), and vertex determination, thus allowing a general survey of single and multi-lepton production.

* Permanent address: Saclay, France

PROPOSAL OUTLINE

1. INTRODUCTION

We propose an experiment to measure single charged leptons (e,μ) and pairs (ee, μμ, μe) produced in pN collisions at the SPS. In addition to charged lepton detection, measurement of the missing energy will provide information on energetic neutrinos, and measurements of secondary vertices will produce important information concerning the charmed, prompt, or other sources of such leptons. We expect to be able to test e-μ universality to the few per cent level, and detect sources of single leptons at the level of a few per cent of the charm contribution for electrons, and at the level of 30% for muons. Good background rejection will allow us to study like-sign as well as unlike-sign pairs.

Powerful detectors are required to achieve this background rejection. The proposed experiment employs novel techniques in triggers, transition radiators, fast high resolution calorimetry, high resolution drift chambers with enhanced multitrack capability, and silicon vertex detectors.

In Section 2 we discuss the physics motivation for this experiment, in Section 3 the apparatus is reviewed, and in Section 4 the experimental procedures are described. A discussion of some specific physics topics is given in Section 5. A detailed description of the various detector components is given in the Appendices.

2. MOTIVATION

2.1 Anomalous Single Leptons

More than ten years have passed since the direct production of leptons was discovered at Serpukhov, Fermilab and the CERN ISR [1]. At the time of their discovery, it was assumed that they originated from a new kind of physics. Today we know that a substantial fraction of them comes from the "new physics" as the term is usually meant: the production of charm and beauty, both open and hidden. Since one is perhaps permitted by the data to suppose that they all originate that way, the sense of urgency has gone out of the effort to understand lepton production in a manner which would withstand a modest quantitative scrutiny.

This situation is illustrated in Fig. 1 which shows measurements of e/π [2] (always excluding low-mass pairs from photon conversions and meson decay). The curves shown are predictions for inclusive leptons from hypothesized sources. For example, at high lepton p_T the measured values are mostly accounted for by leptons from J/ψ, Drell-Yan, and T decays. At lower p_T (less than 1.5 GeV/c) the situation is more confused. The major component of these leptons is often assumed to originate from the decay of charmed particles, particularly the D, or alternatively the measurements are used to evaluate the charmed particle cross-section. There are, however, order of magnitude inconsistencies between lepton measurements and the direct charmed particle cross-sections, and large discrepancies in the experimental results on single leptons and μ-electron correlations [3].

The rise in e/π for $p_T < 0.7$ GeV/c is difficult to explain assuming Dalitz decays have been correctly subtracted, although part of the rise may be ascribed to the anomalous pairs discussed in section 2.4. It has been seen in several experiments, and seems to reappear in production by ν's (see section 2.3).

Experiments at higher p_T at FNAL have shown that some of the leptons are associated with missing energy, as expected from semi-leptonic decays, but the resolution and backgrounds only allow statistical conclusions. Universality in e/μ has been checked to the level of 30% in this region.

Past experience has taught us to regard situations such as this with suspicion, and recently several experiments have pointed to this subject as being of the highest interest.

2.2 Beam Dump Experiments and e/μ Universality

The results of the third round of CERN beam dump experiments have been reported recently (K. Winter, 1983, Cornell Conference), and are given in Table 1. The most significant deviation from universality is found by the CHARM collaboration, which reports the ratio of the number of events due to electron and muon neutrinos, ν_e/ν_μ, to be $0.57^{+0.11+0.07}_{-0.10-0.07}$ [4].

According to conventional ideas, most of these promptly produced neutrinos should come from D meson decay. There are no direct measurements of the e/μ ratio in D decay from the electron storage rings because of the difficulties of muon identification at low energies. In high energy e^+e^- experiments estimates of the $c \to \ell$ and $b \to \ell$ branching ratios have been derived by fitting the p_T distribution of the leptons. However, several other parameters (notably the fragmentation functions) are relevant to the fit, and so the systematic errors are large. The most recent estimates [5] are: MARK II $c \to e$: $6.3 \pm 1.2 \pm 2.1\%$, and MARK J $c \to \mu$: $11.5 \pm 1.0 \pm 1.7\%$.

A value of $\nu_e/\nu_\mu < 1$ was actually predicted by Volkov et al. [6] in an attempt to understand the measurement of a longitudinal polarization in direct muon production [7]. They, Barger et al., and Berger et al. [8], have pointed out that such an effect could arise in heavy quark decay if the emission of a virtual charged Higgs meson is appreciable (Fig. 2). The tendency of the Higgs to couple to massive particles gives the effect of muon dominance and ensures that the influence on light quark decay will be small, but the couplings must be rather special to be consistent with B and τ decay. These ideas seem worthwhile to follow up by a precise experiment specifically comparing electrons and muons from D decay.

2.3 Like-sign Lepton Pairs in Neutrino Experiments

While unlike-sign di-lepton production in neutrino interactions is well understood as charged current production of a single charmed particle, the situation is confused for like-sign di-leptons which have been observed in calorimetric neutrino experiments [9] (μ pairs), and in heavy liquid bubble chamber experiments [10] (μe pairs).

These like-sign di-leptons could come from production of a charmed particle pair, which should be rather similar to associated production in hadron collisions. It has been concluded, however, that these leptons do not originate from this mechanism. Firstly, their rate seems too large. A further check, which is potentially decisive, is to compare the number of strange particles in like- and unlike-sign dileptons with the number

observed in ordinary charged current events. Whilst the unlike-sign pairs show a clear excess, as expected from charmed particle decay, the like-sign pairs do not. The conclusion is that for the like-sign pairs one lepton arises from the charged lepton current and the second comes from the hadronic vertex, but not from a charmed particle decay. However, the statistical evidence is not definitive.

The experiments agree that the characteristics of the "decay" lepton are very similar to those of a typical pion produced in a neutrino interaction, which tends to indicate that the effect, if real, has nothing to do with the properties of the weak current, but is a property of a hadron jet. For example, Fig. 3 shows e/π as a function of the p_T of electrons from neutrino interactions in neon [11], with respect to the rest of the hadrons. This distribution is superimposed on the p_T distribution of electrons at the ISR from Fig. 1. Since the e/π ratios are energy dependent for both p-p and νN interactions, the agreement in magnitude must be fortuitous, but the similarity in shape is striking, and the other kinematic variables tell the same story.

2.4 Anomalous Sources of Lepton Pairs in Hadronic Collisions

The well-understood sources of lepton pairs are nearly real photons internally converting, vector meson decays, and annihilation of quark-antiquark pairs in the Drell-Yan domain. Other sources are known to exist, though the experimental information is very incomplete.

The so-called "anomalous" lepton pairs were observed in a FNAL $\mu^+\mu^-$ experiment [12], which found an excess of pairs below the ρ, compared to those expected from Dalitz decays of η and ω^0. This has been confirmed by several low energy experiments [13]. They have been interpreted variously as thermal radiation, internally converted hadron and quark bremsstrahlung, or non-perturbative quark annihilation. The energy dependence of their production is not well known. It has been argued that they constitute a valuable tool for understanding non-perturbative dynamics [14], and the proposed experiment will put this idea to the test by studying their production in high transverse energy, E_T, events.

Another source of $\ell^+\ell^-$ pairs is the semi-leptonic decay of both members of a $D\bar{D}$ pair. Since essentially all lepton pair measurements are inclusive, this source has long been known to contribute to these measurements, but it has usually been supposed to be negligible. Lack of knowledge of cross-sections and production mechanisms has discouraged attempts to make quantitative analyses, but recently some information has become available. Fischer and Geist have made a very interesting analysis [15] with the somewhat surprising result that reasonable D-$\bar{D}$ cross-sections explain all of the $\ell^+\ell^-$ production in p-p collisions from masses of 2 GeV to over 3 GeV or perhaps much higher, depending on tails of the p_T distribution of the D and possible B production. Measurements of the direct lepton pair cross-section (that is without ν emission) are clearly necessary in order to place the pN Drell-Yan measurements on a sound basis.

3. APPARATUS

3.1 Aims

The considerations of the previous sections have convinced us of the need for a comprehensive study of the origin of charged leptons, neutrinos and neutrino-like objects at the SPS.

The way to carry out such a study is to measure, under as uniform conditions as possible, all the relevant reactions and quantities. This approach requires the use of the following tools, some of which have hardly been employed at all up to now, and never in conjunction:

i) Reliable lepton identification and charge determination with background at the few percent level.

ii) Simultaneous measurement of electrons and muons, both to check μ-electron universality and to exploit the very powerful μ-electron correlation.

iii) Efficient recognition of pairs of charged leptons, so that single charged leptons may be recognized as such.

iv) Of the greatest importance: neutrino measurement (by missing momentum and energy) at the very best accuracy that the techniques and the practical considerations allow.

v) Secondary vertex measurement to allow a completely independent check of the portion of the leptons and neutrinos ascribed to short-lived particles on the basis of the other measurements, and hence to separate prompt, strange, and charm signals.

vi) Ability to trigger on high transverse energy events in order to obtain a separate picture of direct lepton production under these circumstances.

vii) Elimination of lepton background at the trigger level.

These elements are realized in a spectrometer with the layout shown in Fig. 4. Much of this apparatus already exists at CERN. The various detector components are described in more detail in Appendices A-E.

3.2 Detector Components

The apparatus consists of four major components. The Target-Vertex Detector system includes the small target and a silicon detection and trigger system. This is followed by two spectrometers with lepton identifying components. The compact Electron Spectrometer utilizes special drift chambers with high multitrack capability, a "weak field" magnet, transition radiators and fast high resolution liquid argon calorimetry. It is surrounded by a Hadron Calorimeter, for accurate measurement of missing energy. The Muon Spectrometer comprises a magnetic spectrometer and hadron filter. The information from combinations of these components provides the selective triggers and measurement capability necessary for the operation of the experiment.

i) Vertex Detector: The 450 GeV proton beam is focussed on to a beryllium target 50 microns in diameter and 20 mm along the beam direction. The target will see 10^6 protons per second and produce interactions at a rate of 50 KHz. Its size is matched to the precision of vertex measurement by the silicon detectors, essential for reconstruction of secondary vertices. There are three planes of silicon detectors with position resolution of 10μ, and an additional plane subdivided into "pads" which is used for vetoing photon conversions at the trigger level, and is an essential component of the single electron trigger (see Sect. 4.1).

ii) Electron Spectrometer: The high precision (individual measurement resolution 80μ) of the multitrack drift chambers results in a momentum measurement $\delta p/p = 0.001\ p$ (GeV/c) in the "weak field" magnet (0.5T x 1m). The low field integral allows tracks in the Vertex Detector - Electron Spectrometer system to be treated as approximate straight lines for fast trigger purposes, which is a necessary condition for an effective veto of photon conversions by pulse height in the silicon pads. The 8-layer transition radiation detector utilizes cluster readout providing a factor 2000 in hadron rejection. The 15 x 15 mm^2 towers of the first two floors of the liquid argon calorimeter are 8 and 12 radiation lengths deep, respectively, providing a further factor of 200 in hadron rejection.

iii) Hadron Calorimeter: The calorimeter system (composed of uranium-scintillator modules, the uranium liquid argon calorimeter and a calorimeterized iron magnet), is 10 absorption lengths in depth on the beam axis, decreasing to about 4 absorption lengths at large angles, and is designed to achieve a resolution of $\sigma_E/E = 0.28/\sqrt{E(\text{GeV})}$, or about 1.3% at 450 GeV. This will provide essential information on the neutrino spectrum associated with lepton production.

iv) Muon Spectrometer: The threshold for muons to penetrate the total absorption length of the filter is 3.5 GeV. The magnet of (1.7T x 2.5m) combined with the position measuring chambers allows another muon momentum measurement, more precise by a factor of 5 than the Electron Spectrometer. This is important in this "open geometry" muon detection, as tracks in the μ-spectrometer can then be matched to upstream tracks by comparison of momenta (See Section 4.2).

A more detailed description of these components is presented in the Appendices.

4. EXPERIMENTAL PROCEDURES TO SELECT LEPTONS

The primary aim of this experiment is to obtain very pure samples of each of the following processes:

A. Single electrons (e)
B. Single muons (μ)
C. Missing energy trigger (neutrinos)
D. Electron pairs (ee)
E. Muon pairs ($\mu\mu$)
F. Electron-muon pairs ($e\mu$)
G. Lepton neutrino pairs ($\ell\nu$)

We expect to obtain sample sizes of > 20 K for singles, and > 3 K semi-leptonic decays of $D\bar{D}$ pairs.

The experimental problem is simply stated:

- Select leptons (rejecting hadrons)
- Reject background leptons
  (e.g. photon conversions, π, K leptonic decays).

Obviously single leptons pose the more difficult problem; if we can measure singles, then, a fortiori, we can measure the pairs. Accordingly, we shall concentrate on our strategy for obtaining samples of the required size and purity for single electrons and muons.

4.1. Single Electrons

Electron identification at the trigger level.

The single electron trigger begins by demanding a localized energy deposition above some threshold, E_e^{th}, in the liquid argon calorimeter. The fiducial region of the trigger is $6 < r < 30$ cm at the calorimeter face, where r is the radial distance from the beam. This corresponds to an angular coverage of $1.2^0 < \theta < 6^0$. The position of the shower centroid in one projection is then matched to a signal from the 8 layer transition radiation detector (TRD). One can expect a rejection factor against hadrons of 200 from the calorimeter and 2000 from the TRD, giving a combined rejection of 4×10^5 at 5 GeV, improving with energy.

Monte-Carlo studies [16], generating events with a multiplicity 50% higher than the average "minimum bias" multiplicity, show that the event rate from such a trigger is dominated by photon conversions. This is shown in Fig. 5a for an interaction rate of 5×10^4 sec^{-1}, corresponding to 10^6 pps on our target. Note that, for charged hadrons, we have assumed a rejection at the trigger level of only 10^4 in the Monte Carlo.

Rejection of conversions at the trigger level

In order to reduce this rate, the second stage of the electron trigger uses the calorimeter signal and the target centre to make a straight line interpolation to a silicon pad detector situated 15 cm from the target. The basic idea is to reject events in which the selected pad has either no signal, corresponding to a conversion downstream of the silicon and before the TRD, or a twice minimum ionizing signal, corresponding to a conversion before the silicon detector. Since the electron trigger relies heavily on the success of this technique, we itemize here the necessary conditions:

i) The ability to point to a small pad in order to minimize the chance of an overlap with a charged hadron;
ii) The signal from a pad must be such as to allow very efficient discrimination between 0, 1, and 2 particles, see Fig. 6. [17].
iii) The small pad size requires precise pointing from the calorimeter, a small target and a relatively weak field in the region between the silicon detector and the TRD, as one pad dimension must be big enough to allow for the track curvature.
iv) The magnetic field between the target and silicon detector must be sufficiently low to prevent pairs from opening up. We have no magnetic field in this region.

The pad size has been studied with the Monte-Carlo simulation and leads to a design in which the pad is relatively long in the bending direction (4 mm) and short in the other dimension (0.3 mm).

Using the silicon detector to reject events, the trigger rate is substantially reduced, as shown in Fig. 5b. Comparing Figs. 5a and 5b one sees that the silicon detector is very effective at rejecting conversions, which are reduced by a factor of ~ 30, but only mildly effective (factor ~ 2) on π^0 and η Dalitz decays which have much larger opening angles of the pair. This rate is now acceptable for $E_e^{th} > 5$ GeV, and we proceed to consider the further purification of the sample which is performed off-line.

Off-line analysis using track reconstruction, missing energy, and vertex fitting

The off-line purification is performed after track fitting. Monte Carlo studies show that we can then expect a substantial rejection of π and η Dalitz pairs by cutting on such quantities as the 2-particle invariant mass. We also have available the information from the 3 silicon detectors not used in the trigger. The off-line hadron rejection will use the full TRD and calorimeter information to improve this rejection to $\sim 10^6$. Fig. 7 shows the e^+/π^0 background after this first stage of the off-line procedure.

However, we have not exhausted the procedures at our disposal. If we focus on D decay, which we expect to be a major part of the signal (at a level $\sim 3 \times 10^{-5}$ in e^+/π^0), we can now use the total energy measurement to select events in which there is large missing energy, E_ν, carried by the ν. A cut of ≥ 15 GeV missing energy out of a total of 450 GeV brings the total e/π background below 10^{-6} at the lowest electron threshold of 5 GeV (See Fig. 8). For $E_e^{th} > 5$ GeV, Figs. 9 and 10 show the various contributions to e/π as a function of the threshold p_T. It should be noted that since the background decreases with increasing electron energy, we can lower the E_ν cut at higher E_e.

As a further handle on D decays we can search for a secondary vertex resolved from the primary interaction vertex. Appendix B describes the silicon strip detector which gives precise trajectories in one projection, extrapolating tracks to the vertex position with $\sigma \sim [(10)^2 + (70/p)^2]^{1/2}$ μm or about 15 μm for trigger tracks. The 'projection plane' is perpendicular to the silicon strip direction and contains the beam axis.

We also take advantage of the very small target size, 50 μm diameter, which is equivalent to a 12.5 μm standard deviation in the projected distance perpendicular to the beam, comparable to the error on the tracks. We can then take the intersection of tracks with the target to represent the primary vertex, constraining it considerably better than in previous experiments. For example, one track already determines the primary vertex, so that a requirement of at least two tracks on the primary vertex is sufficient to provide a test of its accuracy. Also, the well-identified lepton track is the only one which needs to be assigned to a secondary vertex.

In the detailed simulation of charm particle production, using the ISAJET Monte Carlo, we find that typically 10 tracks traverse the silicon detector planes. These include decay particles from an associated pair of charm particles as well as tracks from the primary vertex. Precise measurement of these trajectories are used to test the hypothesis of a single vertex.

A large χ^2 value for a single vertex hypothesis indicates one or more secondary vertices, and by successively removing tracks from the fit we can attempt to distinguish the decay tracks from those which originate at the primary vertex. Once the main vertex is determined, we can calculate for each track projected on to the 'projection plane':

a) the distance, d, between the main vertex and the intersection of the projected track with a line through the main vertex and perpendicular to the beam axis.

b) the distance, z, between the main vertex and the intersection of the projected track with the beam axis.

Figs. 11a and 11b show the d distributions for D^0 and $D^{\pm}$ decays, respectively. The small target size is clearly important. The average projected miss distance, $\langle d \rangle$, is 0.08, 0.15 mm for D^0 and $D^{\pm}$ decays, respectively. Fig. 12 shows the stretch function, χ_z, for the variable z, where $\chi_z = |z - \langle z \rangle| / \sigma_{\langle z \rangle}$. These distributions illustrate the sensitivity of our vertex system down to 10^{-13} sec in life times.

In our simulation of charm events we find that > 60% of the trigger leptons can be associated with the presence of a secondary vertex by this technique. The remainder includes cases where both charm particles had very short decay lengths, or unfavourable decay angles. The level of charm particle recognition would be raised to ∿ 75% if the silicon detector planes had precise readout in two dimensions.

To summarize the single electrons, we have described a set of trigger and off-line procedures which will reduce the background to a level well below that of the expected signal. For the particular case of D decays we expect to be able to reduce the remaining background to $e/\pi \leq 5 \times 10^{-7}$ for all $E_e > 5$ GeV.

4.2. Single Muons

Muon identification at the trigger level

The 3.5 m path in the Electron Spectrometer, from the target to the liquid argon calorimeter, used to identify and measure electrons, is also a long decay region for $\pi \to \mu\nu$ and $K \to \mu\nu$. These decays constitute the overwhelming background for the single μ trigger. Note that in contrast to electrons, muons deposit little energy in the calorimeter.

The first stage of the single μ trigger is the requirement that a particle penetrate right through to the back of the Muon Spectrometer. The intervening material is 14 absorption lengths, and the punch-through background is already negligible ($< 10^{-5}$). The rate of such a trigger for 5×10^4 interactions per second is $> 10^3$ sec^{-1}, which is much too high. We reduce it using a combination of muon momentum measurements, and missing energy as measured by the calorimeter. The muon momentum is calculated by a micro-processor using the proportional chamber information before and after the muon spectrometer magnet. It should be noted that these proportional chambers are downstream of 10 absorption lengths, and we expect only 1 track in the μ-spectrometer region in ∿ 90% of events. The rate as a function of the threshold momentum of the muon is shown as the upper curve in fig. 13. The effect of requiring a missing energy > 35 GeV is also shown. At high muon energy much of the missing energy inferred from the calorimeter is due to the muon itself. A more effective

procedure is to correct the calorimeter missing energy for the muon energy, demanding that (missing energy - E_μ) > 15 GeV. In this way we obtain a better approximation to the neutrino energy and acceptable single muon rates, as shown in the lowest curve of fig. 13. Furthermore, this procedure parallels the ν energy requirement used on the electron sample.

Off-line analysis

Off-line the purification procedure uses the track information available from the electron spectrometer. We require a match in charge and momentum as measured in the Electron Spectrometer and Muon Spectrometer, allowing of course for the dE/dx loss of the μ as it traverses the 10 absorption lengths before the Muon Spectrometer. In addition, we will be able to reject more than 90% of the $K \to \mu\nu$ decays occurring in the Electron Spectrometer on the basis of bad track χ^2 ("kink rejection"). The remaining background, expressed as μ/charged as a function of μ threshold energy, is shown in Fig. 14.

The use of the vertex information is more important for single muons than for single electrons, because the neutrino energy requirement is less effective. This is because of the large branching ratio for the $K_{\mu\nu}$ decay which readily gives energetic neutrinos. (The $\pi_{\mu\nu}$ does not.)

The acceptance of our detector for D^0, $D^\pm$ leptonic decays is illustrated in fig. 15 as a function of the threshold energy of the lepton [1]. The difference in acceptance between the e and μ decay modes is wholly ascribable to the fact that electrons are not identified in the centre (r < 6 cm) of the liquid argon calorimeter because of the very high multiplicity there. The effect of the missing energy requirement on a $D\bar{D}$ sample is also shown in fig. 15. One sees that a missing energy requirement E_ν > 15 GeV will have an efficiency of $\sim$ 0.5 for the accepted electron or muon sample.

---

1) The $D\bar{D}$ sample was generated by the following two diagrams: $gg \to c\bar{c}$, $q\bar{q} \to c\bar{c}$. We have conservatively assumed that there is no intrinsic charm in the proton. As a consequence the D's are centrally produced: $|y| < 2$, $\langle p_T \rangle \sim 0.7$ GeV/c.

If we assume that the D decay contributions to ℓ/π is $\sim 3 \times 10^{-5}$, the signal to background ratio, after correction for acceptance, is expected to be 2/1 for e/π and 1/3 for μ/π. The missing energy requirement improves these ratios to 30/1 and 3/1, respectively. In calculating these ratios we have used a threshold energy for the accepted leptons of 5 GeV at $\langle p_T \rangle \sim 0.3$ GeV/c.

In summary, we have shown how we plan to trigger on single leptons at acceptable rates. We have also shown that the off-line analysis can reduce the background to a level comparable with the expected signal. The background can be reduced well below the signal if a missing energy consistent with $E_\nu > 15$ GeV is required.

4.3. Missing Energy Trigger

The first level of the trigger requires only a missing energy > 30 GeV. Figure 16 shows the background trigger rate calculated by the Monte Carlo simulation as a function of missing energy, E_ν. We find that this rate is dominated, for $E_\nu > 20$ GeV, by events in which the missing energy is carried by a muon. It is advantageous to introduce a second level trigger which subtracts from E_ν the energy carried by a high energy muon measured in the Muon Spectrometer . The background is then dominated by neutrinos from $K_{\mu\nu}$ decay. If the experimental system works as predicted, and there is no unexpected physical process, this trigger will yield events containing a charged lepton, most of which will be selected by the charged lepton trigger. The rates are then given by the lower curve in fig. 16.

If we look for new physics, one limitation is due to the case where a neutrino is produced with a charged lepton missed in the spectrometer. This occurs about 10% of the time. Should there be an excess of events with missing energy and no charged lepton, there would be a number of physical interpretations: $X \rightarrow \nu\bar{\nu}$, SUSY particles etc. We have the possibility of examining the associated particles produced in the event, short-lived particles, energy flow, etc. for additional clues.

4.4. Pairs of Charged Leptons

As mentioned above, the capabilities of this apparatus to measure single electrons and muons implies that pairs can be analyzed with reduced background and/or more relaxed triggers and off-line cuts.

At the trigger level, acceptable rates for pairs can be achieved by:

electrons: TRD association with e.m. shower in the calorimeter for $E_e > 5$ GeV

muons: Muon Spectrometer microprocessor momentum cut of $P_\mu > 5$ GeV/c and penetration of the hadron filter.

The rates for charged lepton pairs are shown in fig. 17. These rates are dominated by background from π and K decay, conversions, Dalitz decays etc. The rate for $\rho \to \mu^+\mu^-$ is ~ 0.7 sec^{-1} and for $\rho + \omega \to e^+e^-$ is ~ 1 sec^{-1}.

Although these rates are acceptable, we can impose a missing energy requirement of $E_\nu > 15$ GeV, correcting for muons as already described, which reduces the rates by a factor of ~ 10 (see fig. 16). Such a cut has little effect on the $D\bar{D} \to$ di-lepton events, as illustrated in fig. 18.

5. PHYSICS ANALYSIS

5.1. e/μ Universality:

Charged lepton pairs:

We consider first the case that the e/μ non-universality indicated by the CHARM beam dump experiment is due to unequal branching ratios of D's to electrons and muons. Then the best way to observe the effect in our experiment is to deal with opposite-sign lepton pairs, e^+e^-, $e^\pm\mu^\mp$ and $\mu^+\mu^-$. Because of the associated production of D's and the relatively large leptonic branching ratios, there is a strong correlation between the decay leptons which, combined with our good lepton identification, causes the background to be very small in the unlike-sign dileptons, even for $\mu^+\mu^-$. This can be checked by comparing with the like-sign dileptons. The results of the experiment can be displayed in a manner which is manifestly free from a critical dependence on corrections from event simulation.

Let the probability of $D \to \mu$ be P_μ, and of $D \to e$ be P_e. Then associated production of D's will result in e pairs and μ pairs in the ratio:

$$T_1 = P_e P_e / P_\mu P_\mu .$$

The ratio of $e\mu$ pairs to μ pairs is $P_e P_\mu / P_\mu P_\mu$, and hence

$$T_2 = (P_e P_\mu / P_\mu P_\mu)^2 = T_1$$

Experimentally we shall consider the ratios:

$$R_1(E_\nu) = \frac{Ne^+e^- - Ne^\pm e^\pm}{N\mu^+\mu^- - N\mu^\pm\mu^\pm}$$

$$R_2(E_\nu) = \left[\frac{Ne^\pm\mu^\mp - Ne^\pm\mu^\pm}{N\mu^+\mu^- - N\mu^\pm\mu^\pm}\right]^2$$

where the ratios and the numbers, N, of the various lepton samples taken with the pair trigger, with no vertex or missing energy requirements, are functions of the missing energy measured by the calorimeter, E_ν. We have argued that the backgrounds in the unlike-sign pairs are small, but we subtract them, as estimated from the like-sign pairs.

For the Drell-Yan process or ρ, ω, ϕ and J/ψ decay, $R_1 = 1$ and $E_\nu = 0$. For $E_\nu = 0$, R_2 should tend to zero. Given our elaborate trigger and analysis procedures, the uncorrected $R_1(0)$ is not expected to be equal to one. Rather than trying to calculate a correction factor with the required precision, we shall simply normalize $KR_1(0) = 1$ defining K. Provided we take care to match the kinematic distributions at different E_ν, e.g. the p_T, p_L, and $m_{\ell^+\ell^-}$ distributions, and given that E_ν is always a small fraction of the beam energy, we do not expect the factor K to depend significantly on E_ν. With our planned samples of $N_{e^+e^-} = N_{\mu^+\mu^-} = 2 \times 10^4$ for $E_\nu < 5$ GeV, and $N_{e^+e^-} = N_{\mu^+\mu^-} = N_{e^\pm\mu^+} = 3 \times 10^3$, for $E_\nu > 15$ GeV, and small backgrounds, the statistical errors on R_1 and R_2 should each be about 2%, corresponding to a 1% error in e/μ ($= \nu_e/\nu_\mu$). If we find $R_1 = R_2$ at non-zero E_ν, then that would be powerful confirmation that the various unlike- sign pairs are indeed coming from some source like $D\bar{D}$.

It may be that $\nu_e \neq \nu_\mu$ but the origin is not D decay. In that case we must consider further possibilities. Some of them will show up in the above analysis. Note that the samples used in the above analysis did not have the vertex cuts applied. If the events with E_ν > 10 GeV are dominantly due to D decay, as expected, the events will show a very strong correlation with secondary vertices with the D lifetime. If the ν_e/ν_μ problem is due to the decay of some other particle, it may well have a quite different lifetime, and that will be strikingly evident. Generalizing this approach we would study $R_1(z_\ell)$ and $R_2(z_\ell)$, where z_ℓ is the projected miss distance along the beam axis, described in section 4.1. Since z_ℓ is zero for Drell-Yan and vector meson decays, the normalization trick can be used without reference to neutrinos. This leads to a e/μ universality test for particles with lifetimes in the range 10^{-10} sec to 10^{-13} sec, independent of neutrino energy.

Charged single leptons

If we see no effect in the pair analysis, the source of the beam dump anomaly will show up in singly produced charged leptons, provided that each charged lepton is associated with a ν of the same flavour. We can use the single charged lepton data sample to measure e/μ, which is expected to be 1 if there is no anomalous source. Our sensitivity to any anomalous source depends on the lifetime and decay kinematics of such a source, for which we have no model. We shall now consider the cases in which this lifetime is comparable to the D lifetime, or much shorter.

For the first case the requirement that the lepton come from a secondary vertex (described in section 4) retains 60% of the D's while reducing the background by a factor 15. After this selection, both the single electron and single muons have backgrounds of less than 2%. The statistical error on e/μ is ∿ 1%. The acceptance correction factor for e/μ is $(K)^{1/2}$ to an accuracy of ∿ 2%, where K is determined from $R_1(E_\nu = 0)$. The final error for e/μ in this analysis is expected to be ∿ 3%. Hence we have a sensitivity at the level of a few percent of D production for an anomalous source whose lifetime is > τ_D.

For the second case, in which the ν source does not have a recognizable lifetime, one must work with the single lepton samples without vertex analysis. One is limited by the background in the muon sample, which is about 30% of the signal. This can perhaps be determined with a relative error of 50% or 15% of the signal, by event simulation and observation of cases like $K^o \to \pi\pi$, $\pi \to \mu\nu$ as well as $K_{\mu\nu}$ decays with identified decay vertices in the range $10^{-12} < \tau < 10^{-10}$s. This will then determine e/μ with an error of about 15%.

No charged leptons

Finally, we must consider the possibility that the anomaly arises from a source which does not produce charged leptons, e.g. $\nu_\mu + \bar{\nu}_\mu$. In order to produce the observed effect, this source would have to occur at about 50% of the rate of leptonic D decay with a similar energy spectrum. If it really produces two neutrinos, then, for our missing energy trigger $E_\nu > 35$ GeV, it will account for the majority of the events. Given that for D production with $E_\nu > 35$ GeV we observe the lepton 90% of the time, this case in which no lepton is produced should be readily recognizable as an excess of leptonless events. Such measurements have been made, in the guise of searches for production of supersymmetric particles, but in our case the calorimeter resolution of 28%, almost three times better than in the experiment of Bodek et al. [18], allows detection at the level of D production, as shown in Section 4.3.

In summary, our experiment is sensitive to most mechanisms which could account for ν_e/ν_μ at the level found by CHARM, and would be sensitive to much smaller deviations from universality for the more conventional sources such as D decay.

5.2. Sources of Anomalous Single Leptons

We believe our good identification of leptons, particularly of electrons, can contribute to our knowledge of the inclusive spectrum, which is poorly known at low p_T. More important, we can measure the missing neutrinos and secondary vertices on each event. We thereby expect to see if there really is a rise at low p_T, and to see how much is due to charm production, how much to low mass pairs, and whether these are the only sources.

5.3. Studies of Anomalous Low Mass Pairs

Our technique of momentum matching between the Electron Spectrometer and the Muon Spectrometer allows us to measure muon pairs with good mass resolution down to $m = 2m_{\mu}$. The trigger requirements on electron pairs cut off the acceptance below a mass of 200 MeV/c^2. In the range 200 - 500 MeV/c^2, the η and ω Dalitz decay may make an important contribution. This can be determined directly by measuring the associated photon, which is emitted close to the momentum vector of the pair, in the small towers of the forward calorimeter. Between 200 and 650 MeV/c^2, the indications are that there is an "anomalous" signal about 10 times that expected from the tail of the ρ/ω and hadron bremsstrahlung internal conversions. The shape is not known quantitatively: is it the tail of a real photon component, or is there a broad peak around masses of 300 MeV/c^2? This experiment should settle that question. We will also measure the transverse energy, E_T, associated with these photons. If they can be interpreted as a kind of thermal radiation, they should be associated particularly with the large number of degrees of freedom excited in such events, and may prove to be the best way to characterize these states. We may wish to examine a small amount of data on low mass pairs taken with a heavier nucleus as the target and a high E_T trigger.

5.4 Studies of High Mass Pairs.

We take "high mass" to mean the region above the ρ/ω. In this region, particularly around 1-3 GeV/c^2, there is doubt as to the direct pair production cross-section, because of the contamination from charmed paticle decays. We have indicated in section 5.1 how we plan to separate these contributions. The result could well be that the Drell-Yan cross-section explains the pair production down to lower masses than previously thought. It could also be that the Drell-Yan contribution to the cross-section in the 4 GeV/c^2 region is lower than the presently accepted values. In order to extend the mass region, we could accept massive muon pairs produced in interactions in the liquid argon calorimeter ('beam dump'). These will include some secondary interactions, but they will not interfere with the determination of the true pair fraction from the missing energy measured in the calorimeter.

APPENDIX A

Beam and Target

We need a target of very small diameter for two reasons, to reduce the photon conversions and to increase the effectiveness of secondary vertex measurements. Both considerations point to a diameter of the order of 50 μm. In order to have a reasonable targeting efficiency, the beam must be of comparable size.

The emittance of the SPS beam, combined with the focussing power of the standard quadrupoles, does not allow the full beam to be focussed to a spot with diameter smaller than 300 μm. However, we need only a very small fraction of the full beam, so emittance slicing suggests itself. Such a large reduction can only be achieved in several stages, however, and only a few SPS beams have sufficiently flexible optics. The best candidate is the H8 beam in the North Hall. A design has been worked out by H. Atherton and N. Doble. This uses the existing beam with the addition only of two new slits. It can provide more than 10^7 particles in a round spot with σ = 30 μm. A clean-up focus is provided so that the halo around the spot should be reasonably small. This is not so important in event analysis, but we want to minimize radiation in the silicon. Experience with beams with 100 μm vertical dimension in the North Hall gives no evidence of problems with positional stability over periods of the order of a day.

The target itself will be a wire supported by a spider on a frame with the well-aligned silicon detector. This will also carry a small tungsten collimator, ID 400 μm, OD 5mm, length 36 cm, to protect the detectors in case of beam miss-steering. It is preceded by a fixed collimator with a 3 mm aperture.

APPENDIX B

Vertex Detector

The vertex detector is a set of three planes of silicon strips, and one plane with pad readout. The polar angle coverage is 8° and the strip planes are at 100, 125 and 200 mm from the centre of the target, and the pad plane is at 150 mm. The thickness of each is 300 μm.

The pad plane is vital to achieve a satisfactory trigger rate for electrons, by eliminating the overwhelming majority of the photon conversions and a significant fraction of internal conversion pairs by demanding a single particle at the position predicted from the observation of the electron in the calorimeter and the TRD (see section 4.1). The size of the pads is adapted to the accuracy of this prediction, and is 4.0 mm in the direction perpendicular to the magnetic field in the electron spectrometer magnet and 0.3 mm along the magnetic field. The detector capacity is evidently quite small, and the resolution is determined by ionization fluctuations. A recent measurement in a silicon detector of the same thickness is shown in Fig. 6. The trigger window would be set to give a single electron efficiency of $\sim$ 90% and rejecting > 99% of pairs contained in the pads.

The silicon strip planes contain an array of strips parallel to the spectrometer magnetic field. (A development is underway to see if it is practical to provide an orthogonal array of strips on the opposite face of the same silicon wafer). The spacing of the strips near the beam axis is 80 μm, fixing the particle pair resolution at 160 μm. The central strips are broken into two halves, independently read out, by a 400 μm diameter hole which allows the beam to pass through without interacting or causing radiation damage. The effective diameter of the dead area is 1000 μm.

The particle position between strips is interpolated by charge division [19]. Prototype detectors have been studied using a micro-beam of 3 MeV protons to establish the construction techniques. The differential linearity achieved in this technique provides 5 μm accuracy in a fully depleted detector.

The detector and the target will be mounted on a ceramic frame with relative alignment by optical means to an accuracy of 3 μm. This assembly needs to be aligned parallel to the proton beam axis with an accuracy of 0.5 mrad, which should not be difficult since the whole aperture of the last quadrupole as seen at the target is about 2 mrad.

APPENDIX C

Electron Spectrometer

It is the task of the electron spectrometer to momentum analyze the charged particles, and to track electron candidates from the Si-detector to the transition radiation detector and the electromagnetic calorimeter. Electron identification is provided in the eight-layer TRD and the electromagnetic front section of the calorimeter.

The compact size of the spectrometer and the weak magnetic field ($\int Bdl \simeq 0.5$ Tm) determine the required performance of the tracking chambers. Adequate momentum resolution, $\Delta p/p \leq 10^{-3} p$ (GeV/c) implies a spatial resolution of $\sigma \leq 100$ μm. A more severe criterion is imposed by the particle density in the interesting events. Based on Monte Carlo studies we estimate that the corresponding two-track separation, Δ, has to be less than ~ 600 μm to keep the loss of unreconstructed tracks at the 5% level. These two performance criteria are very severe for present day technology, and place the required track detectors in the vertex detector category.

The following parameters have to be suitably controlled to achieve this performance [20]:

- use of a "cool" gas, e.g. CO_2, to minimize diffusion;
- an isochronous drift chamber geometry to minimize drift time differences from different track-segments projected onto the same sense wire;
- suitable pulse shaping [21] to minimize the effect of the positive ion tail.

We have constructed a small prototype chamber and tested it with laser pulses and in the high-rate environment of the ISR to study the practical realization of such a detector (See Fig. 19). The chamber was operated with 100% CO_2 at STP, and gave the following performance [22]:

$\sigma_x = 90$ μm for a drift of 1cm (Fig. 20).

$\Delta = 600$ μm (Fig. 21).

30 The mechanical realisation of such a chamber, which is based on the successful method employed for the AFS vertex detectors, allows scaling to larger dimensions without deterioration in performance. We are presently computer optimizing the settings of the electrical potentials, evaluating the choice and operating conditions of the drift gas, and considering other chamber geometries with a potentially even better performance.

The principal contributors to this successful development were P. Frandsen, P. Queru, E. Rosso, A. Rudge, and D. Soria-Buil and we expect that these people will be available for the preparation of the full size chambers.

The sense wire geometry considered is sensitive to one side only and hence eliminates any problem of left-right ambiguity. Longitudinal coordinate information is obtained with small angle stereo of 5°. For best π- and K-decay recognition high resolution along the magnetic field direction is also necessary. This is easily achieved by alternating the drift chamber modules by 90°. The "super module" therefore will be equipped with eight sense wire planes, oriented along x, $x + \delta x$; u, $u + \delta u$; y, $y + \delta y$; v, $v + \delta v$. We envisage for momentum measurement purposes to install four such super modules before and four behind the dipole magnet. The momentum resolution which can be achieved with such a spectrometer configuration is calculated to be $\Delta p/p < 10^{-3} p$ (GeV/c), not including the multiple scattering (m.s.) contribution evaluated to be $\Delta p/p \simeq 1.5 \times 10^{-2}$. Limitations are likely to arise from incomplete knowledge of systematic corrections, although for several years we have practised laser calibrations of drift chambers. We allow for some degradation and estimate $\Delta p/p = 10^{-3} p$ (GeV/c) + m.s. contributions.

The dipole magnet is of conventional construction, with a cos θ current distribution in normal-conducting coils, integrated with the magnetic calorimeter. We prefer a design with moderate power consumption and conservatively consider therefore a magnetic field of 0.5 T over the length of one metre. The instrumented "nose" of the magnetic calorimeter is sufficiently long to shield effectively the magnet coils, thus preventing any loss in acceptance. In a similar way the support frame of most of the tracking chambers can be located outside the nominal spectrometer acceptance, again shielded by the nose-calorimeter. Only the small most forward chambers will require a more careful integration.

The Transition Radiation Detector (TRD)

The transition radiation detector is designed to achieve sensitive discrimination between electrons and pions ($e/\pi \leq 10^{-3}$ to 10^{-4}) for electrons above $p \sim 5$ GeV/c, already at the first level trigger stage. Such designs have become practical with the development of the TR-cluster counting method. In this method the separation between the ionization energy loss and the localized energy deposit, caused by the absorption of TR-photons, is enhanced by analyzing the time dependence of the induced charge signal on the anode wires of a MWPC-type TR-detector. In its simplest and most powerful form, TR-cluster counting is achieved by counting the number of localized energy deposits (recognized as a fast current pulse) above a certain fixed threshold. This can be achieved with rather conventional preamplifier/discriminator circuitry and is the basis for electron discrimination and triggering. For additional discrimination the position of the electron candidate as measured by the TRD is spatially correlated with electromagnetic showers in the calorimeter (see Appendix F "Trigger").

We have studied a number of radiator/detector combinations with a view to optimizing the electron/pion discrimination, while keeping the overall length small and the total amount of radiator material tolerable [23].

Various materials are being considered as radiators. Our quoted rejection is conservatively based on the use of carbon fibres, although a somewhat better performance can be expected by using polyethylene fibres (M. Holder, private communication).

APPENDIX D

Calorimeters

We plan to measure the energy flow as well as possible to obtain accurate information on the produced neutrino or neutrinos. Most of the energy in typical events is of course contained within the cone of polar angle 6° subtended by our forward calorimeter, and that device will be described first, but our event simulations show that coverage of large angles is also necessary to measure the tails on the missing energy and missing transverse momentum distributions.

Uranium-Liquid Argon Calorimeter

The forward calorimeter should deal with a rate of 1 MHz of beam particles in a small spot, while measuring the energy with a precision approaching 1%. We also wish to measure the transverse centroid of the energy flow with good precision in order to determine the p_T of a missing neutrino. Finally, the electron showers must be detected cleanly in a high multiplicity environment. These requirements demand a design with fine sampling and fine grained segmentation in all three dimensions, while preserving a good uniformity. The best way to achieve these aims is with a liquid argon ionization chamber readout. The resolution desired for incident hadrons requires the use of a uranium absorber. The short response time needed implies some innovations in the design of the liquid argon readout, and some prototype work has been done to verify the feasibility of the design.

The unit cell of the calorimeter is a 1.75 mm plate of uranium, followed by a 1 mm gap of liquid argon, a 1 mm printed circuit electrode, and another 1 mm of liquid argon. The liquid argon gap is maintained by a plastic honeycomb spacer of cell size about 10 mm, a technique we have used in large devices previously. The electrode structure consists of towers in the first 20 radiation lengths, subdivided into 8 and 12 radiation length sections. The towers are 15 x 15 mm^2. The remainder of the calorimeter, 4.5 absorption lengths long, is segmented in 15 mm wide strips, interleaved in orthogonal projections. It is divided into four longitudinal sections. Each longitudinal subdivision is further divided in the readout into two independent interleaved outputs, in order to

provide a cross-check of calibration faults and other detector malfunctions, or rare extremes in sampling fluctuations. In this way, we expect that the resolution function should remain Gaussian into the tails where the energy carried by penetrating particles (muons) starts to dominate, as discussed in the main text.

The fast response time can be achieved with attention to low inductance connections, use of liquids faster than pure liquid argon, and careful shaping of the signals. Mock-ups of the calorimeter and its connections have been built to confirm their suitability for transmission of fast signals. The liquid to be used is argon plus 1% methane, which gives a saturated mobility three times that of the pure liquid. Such mixtures are more sensitive to electronegative contaminants than pure liquid argon. We have studied the purification procedures necessary to retain the same (or slightly higher) charge signal as in liquid argon. More careful control of construction materials than in the usual case seems to be necessary.

The shaping we plan to use is approximately a bipolar Gaussian with each lobe 50 ns long. This implies cancellation of some of the charge collected, and is possible in our case because of the small fluctuation in the shape of the signal current, and the relatively large energy being measured compared to the noise, which is estimated to be about 1.5 GeV for the whole calorimeter.

Our measurements in a calorimeter with the same plate thickness and ratio of liquid argon to absorber gave a resolution on contained energy of $\sigma_E/E = 0.28\ E^{-1/2}$ (GeV), i.e. 1.3% for 450 GeV. We have found that calibration and uniformity can be better than 0.3%, which will be verified directly by means of the interleaved readout.

Uranium-Scintillator Calorimeter

The liquid argon calorimeter is by no means deep enough to contain such a high energy cascade. About 10% of the energy will leave the back of the calorimeter and pass into an array of our uranium-scintillation calorimeter modules. These have a resolution, for fully contained energy as in this case of $\sigma_E/E = 0.34E^{-1/2}$. The errors of uniformity and calibration are about 1.5%, and they do not have the required spatial segmentation to function as the main calorimeter, but they are adequate to

measure the leakage from the front calorimeter without degrading the overall result, and a great economy is made by using them. The total thickness of this array is 5.5 absorption lengths, and that of the whole absorber is 10 absorption lengths. Events will be discarded where the energy in the last two absorption lengths is more than 5 GeV. This should ensure correct measurements of missing energy, and a clean pattern in the muon spectrometer.

Our Monte Carlo simulation indicates a precision on the transverse momentum balance of about 0.3 GeV/c. We have no experimental verification of this number, and we have not used it in our description of the procedures we expect to follow. Clearly, if the actual number is at all near this prediction, we will have another powerful tool for measuring neutrinos, and we intend to ensure that this error is as small as possible. The simulation shows that this error particularly, as well as the tails on the missing total energy, are sensitive to the measurement of energy emitted at large angles. Accordingly, we have provided for a large angular coverage with essentially no cracks.

Calorimeters at Large Angles

There are three elements in this coverage: the small "cone calorimeter" shadowing the dipole coils, the calorimeterized iron in the dipole itself, and the uranium-scintillator modules covering the large angle region. The cone calorimeter covers polar angles between 6° and 8.6°. Its 50 cm of Cu absorber is read out with silicon wafers to give a resolution of $\sigma_E/E \simeq 0.7\ E^{-1/2}$, segmented in 24 azimuthal towers. Between 8.6° and approximately 16°, the energy is measured in the iron of the dipole by scintillators inserted in slots separated by 2 cm of iron and read out by wave length shifter bars, with resolution of $\sigma_E/E = 0.8E^{-1/2}$. Much of the energy will pass through the exterior surface of this iron and be measured in the uranium calorimeter which surrounds it. This is composed of our existing uranium-scintillator modules, with resolution $\sigma_E/E = 0.37/E^{-1/2}$ covering angles up to 90°. The angular region from 9° to 49° is also covered by an array of NaI crystals, largely from experiment R808, whose function is to measure photons from large E_T events, in correlation with anomalous lepton pairs.

APPENDIX E

Muon Spectrometer

We propose to use the existing NA3 spectrometer as our muon spectrometer. Our forward calorimeters replace the previous dump by providing 10 absorption lengths of active beam dump and hadron filter. We summarize the relevant features of the NA3 spectrometer in its unmodified form and indicate a minimum configuration.

Unmodified NA3 Spectrometer [24]

The general layout is shown in Fig. 4. The large acceptance magnetic spectrometer has a momentum resolution of $\sigma_p/p^2 = 0.02\%$ and consists of

- a large superconducting dipole magnet with vertical field (1.7T x 2.5m) in an air gap of cylindrical shape of 1.6 m diameter.
- a set of seven multiwire proportional chambers ranging in size from 0.3 x 0.3 m^2 up to 4.2 x 4.0 m^2, covering vertical angles from ± 6 mrad to ± 165 mrad. (These chambers formed the basis of the NA3 large p_T or large dimuon mass trigger).
- a pretrigger determined by three planes of horizontal strip counter telescopes: T1, T2 and T3. The last two hodoscopes cover vertical angles from ± 6 mrad to ± 155 mrad. The pretrigger requires at least 2 particles in the coincidence T2, T3 and at least one in T1, geometrically pointing towards the target.
- an on-line processor which calculates the effective dimuon mass for a large fraction of the events.

Minimum Configuration

While the unmodified spectrometer is usable as such (see Appendix "Trigger", however, for our different triggering scheme), a simpler and more compact minimum configuration can be defined which increases the acceptance while providing a lower p_μ cut.

APPENDIX F

Trigger

We may consider the trigger system under the following headings:

1. VFB System for parallel triggers
2. Analogue processing for energy flow
3. Momentum measurement in muon spectrometer
4. Electron trigger.

The collaboration possesses equipment which can be adapted to carry out most of these functions, but some new items will be built.

1. The VFB stands for 'very fast bus', a system which was built to handle many parallel triggers for the Axial Field Spectrometer at the ISR. Its structure is very flexible, and it can be adapted for the present experiment with some reworking of the mechanics and software and the construction of some special modules. This will allow the different triggers to work in parallel under computer control and with computer verification of the trigger requirements.

2. A system for processing calorimeter signals is included in the VFB. It will be adapted for the different geometry of the present experiment and extended to accept inputs from the additional calorimeters. It will provide fast measurements of missing energy and p_T balance, E_T, and high p_T. The liquid argon calorimeter will provide some analogue energy flow processing within its own electronics, so that the modifications to the existing system will be minimized.

3. Momentum measurement in the muon spectrometer. A fast measurement of the single muons in this spectrometer is needed in order to correct the measurement of missing energy due to neutrinos. (On the other hand, pairs of all masses will be recorded, in distinction to high mass pair experiments). The collaboration is studying the merits of ESOP and MICE processors for this purpose.

4. The electron trigger requires defining an energy threshold on localized energy in the calorimeter, and determining its centroid in two dimensions, correlating this with a localized signal in the TRD and making a final correlation with the appropriate pads in the silicon pad detector. A study has been made of a system which determines localized energy thresholds and projections in two orthogonal projections in the calorimeter. Just such a system was built for R806 and it might be reused. It even included a correlation with a TRD detector which is required in our case as well. The correlation with the silicon pads and the resolution of stereo ambiguities in the calorimeter would be done by matrix look-up.

APPENDIX G

Schedules and Responsibilities

The scope of the proposed experiment and the necessary preparation for it are of course closely linked to the expected Fixed Target Operation Schedule of the SPS. Recently, the Research Board decided on September 1984 for the start of the next $p\bar{p}$-Collider period. Following the very positive experience with the last $p\bar{p}$-runs it is plausible to expect this period to extend over approximately one year, placing the start-up of the subsequent FT period in the fall 1985, which in turn might last approximately one year. It is this period, from fall 1985 to fall 1986, during which the proposed programme has to be carried out.

During the coming two years the following systems have to be developed and constructed, and we propose to share the responsibilities among the collaborating institutions in the following way:

Beam: A detailed design has been studied for the H8 beam by our collaborators from the SPS division, which would carry out the necessary modifications.

Vertex Detector: BNL is proceeding with prototype studies on the Si-Detectors. They have demonstrated their in-house capability to fabricate these devices. The BNL-Instrumentation Division will also be developing the preamplifiers, and be responsible for the packaging of the complete vertex detector.

Precision Drift Chambers for Electron Spectrometer: The very successful prototype work, which demonstrated the feasibility of the required performance, was carried out at CERN. Successful construction of the final chamber hinges to a large extent on the use of construction techniques pioneered at CERN, and we therefore request CERN to take the responsibility for it.

The Magnetic Calorimeter and Dipole Magnet: The calorimeter, which uses scintillators and BBQ readout, requires engineering and machining capabilities and a staff used to careful assembly and testing. We expect Rutherford to carry out this effort.

The Liquid Argon Calorimeter: This is the major new component and the one which requires the longest lead time. The successful prototype tests and study of the delicate signal processing system were carried out by BNL, which has agreed to construct the calorimeter and to pay for the electronics. We know from past experience that such instruments require in addition some CERN support of people experienced in this kind of detector, and who in particular are concerned with the systems integration of the cryogenics and the signal processing electronics.

The Uranium Scintillator Calorimeters: We do not expect to encounter any major problems with reusing the R807 calorimeter modules and its associated Computer controlled HV system, which have been working flawlessly for a long time at the ISR. The units will however require recalibration, maintenance, and perhaps some work on the scintillators. We would expect that members of the CERN team, who originally built this device, would be available for this task.

The Transition Radiation Detectors: The design is based on work of the CERN/Moscow Collaboration. Our Moscow collaborators (The Lebedev Physical Institute and the Moscow Physical Engineering Institute) will share the responsibility for the fabrication and tests of the radiators and the proportional chambers.

For the read out of the chambers we plan to reuse the R807 Drift chamber preamplifiers and its DTR system for the cluster counting. The possible reuse of the R807 shaping amplifiers for the charge measurements and the integration into the electron trigger system are under study.

The On-line System: We plan to use a data acquisition system based on a VAX-Computer, which will be provided by Syracuse University. The Camac System will be modelled on the R807 system, which was studied and found adequate for the task. The data acquisition and monitoring programmes will be standard CERN packages, as currently used for example on the Omega spectrometer.

Electronics Support: Despite the extensive reuse of R807 electronics and trigger systems, an experiment of this scope needs a team of electronics engineers and technicians to prepare and support the signal processing and trigger system, with experience both in precision analogue and high speed digital electronics. We request that the small "force de frappe", who masterminded the complex R807 system, should be available to continue to carry out the required changes of and additions to the R807 system, and be responsible for the systems integration.

Table 1: Recent beam dump results

Exp.	ν_e/ν_μ	E_ν threshold
BEBC	$1.35 \pm {}^{0.69}_{0.34}$	20 GeV
CDHS(prel.)	$0.83 \pm 0.13 \pm 0.12$*	20 GeV
CHARM	$0.57 \pm {}^{0.11}_{0.10} \pm 0.07$	2 GeV
FMOW	$1.02 \pm 0.09 \pm 0.1$	20 GeV

*) This value reduces to 0.76 if the same corrections on target density are applied as used by the CHARM Collaboration.

FIGURE CAPTIONS

Fig. 1 The e/π ratio as measured at the ISR. Also shown are the measured contributions from Drell-Yan, J/Ψ, and T production, as well as the lepton yield from open charm and beauty production.

Fig. 2 Diagram for c quark decay via a charged Higgs.

Fig. 3 The same sign electron/pion ratio, as measured in νp interactions [11].

Fig. 4 Side view of the experimental setup
a) The full experimental setup.
b) Detail view of electron spectrometer.

Fig. 5 Single electron trigger rates, assuming 10^6 pps and 5×10^4 interactions sec^{-1}, as a function of electron energy threshold.
a) Trigger rates using only the calorimeter and the TRD.
b) Trigger rates using the calorimeter, TRD, and silicon pads.

Fig. 6 The energy loss spectra in a silicon detector of 300 μm thickness for 115 GeV/c incoming proton momenta. The tail is shown with the vertical scale multiplied by ten [Ref. 17].

Fig. 7 e/π ratio from various background contributions as a function of electron threshold energy, after off line analysis.

Fig. 8 As Fig. 7, but requiring in addition a calorimeter missing energy > 15 GeV.

Fig. 9 e/π ratio from various background contributions, after off-line analysis, as a function of the transverse momentum threshold of the electron. Electron energy threshold > 5 GeV.

Fig. 10 As Fig. 9, but requiring in addition a calorimeter missing energy > 15 GeV.

Fig. 11 Distribution of the distance d for D^0 (11a), and $D^{\pm}$ (11b).

Fig. 12 Distribution of the stretch function χ_z. The two curves are for tracks from D decay and tracks originating from the main vertex.

Fig. 13 Single muon trigger rates, assuming 10^6 pps and 5×10^4 interactions sec^{-1}, as a function of muon energy threshold. The lowest curve corresponds to the rates when a calorimeter missing energy (with observed muon energy subtracted) > 15 GeV is required.

Fig. 14 μ/charged ratio from π and K decays as a function of muon threshold energy after various off-line requirements;
a) a χ^2 selection for kink rejection in the forward spectrometer.
b) requirement of a momentum balance between the muon as measured in the electron spectrometer (p_1) and in the muon spectrometer (p_2).
The lowest curve represents the expected off-line μ/charged ratio when a calorimeter missing energy (with observed muon energy subtracted) > 15 GeV is required.

Fig. 15 Acceptance for D^0, $D^{\pm}$ leptonic decays for different missing energy cuts as a function of:
a)electron trigger threshold
b)muon trigger threshold .

Fig. 16 Trigger rates with calorimeter missing energy > 30 GeV. The lower curve shows the rate when the calorimeter missing energy requirement is modified to allow for the energy carried by the muon.

Fig. 17 The raw trigger rate for charged lepton pairs μμ, μe, ee as a function of the lepton threshold momentum.

Fig. 18 The acceptance for $D\bar{D}$ pairs triggered on charged leptons as a function of lepton threshold momentum, with missing energy cuts of 15 GeV and 30 GeV.
a) $\mu^+\mu^-$ pair, b)$\mu^{\pm}e^{\mp}$ pair, c) e^+e^- pair.

Fig. 19 Wire configuration of the prototype chamber. S is the sense wire (30 μm), C the "channelling" wire defining the length of the accepted track segment, P is the potential wire decoupling adjacent sense wires, G is a gate wire to provide single drift sensitivity and additional gain control for the sense wires.

Fig. 20 Resolution and pulse height versus drift distance. ISR test results.

Fig. 21 Distribution of two-track separation obtained from an ISR exposure of the prototype chamber. Full scale is 6000 μm.

REFERENCES:

[1] M. Banner et al., Phys. Lett. 44B (1973) 537;
S. Nurushev et al., Proc. 17th Int. Conf. on High-Energy Physics, London (1974) V 53;
J.P. Boymond et al., Phys. Rev. Lett 33 (1974) 112;
F.W. Büsser et al., Phys. Lett. 53B (1974) 212;
V.V. Abramov et al., Phys. Lett. 64B (1976) 365;
L. Klugberg et al., Phys. Rev. Lett. 37 (1976) 1451.

[2] The compilation is due to P. Baillon et al., CERN/SPSC/82-55;
with data from:
L. Baum et al., Phys. Lett. 60B (1976) 485;
F.W. Büsser et al., Nucl.Phys. B113 (1976) 212;
M. Barone et al., Nucl. Phys. B132 (1978) 29;
M. Basile et al., Nuovo Cimento 65A (1981) 421.

[3] D. Treille, Proc. Int. Symp. on Lepton and Photon Interactions at High Energies, Bonn (1981) 750;
A. Clark et al., Phys. Lett. 77B (1978) 339;
L. Baum et al., Phys. Lett. 77B (1978) 337.

[4] P. Fritze et al., Phys. Lett. 96B (1980) 427;
M. Jonker et al., Phys. Lett. 96B (1980) 435;
H. Abramowicz et al., Z. Phys. C13 (1982) 179;
K. Winter, Beam dump results; Talk at the 1983 Int. Symp. on Lepton and Photon Interactions at High Energies, Cornell, August 4-9, 1983.

[5] MARK II result from:
'Review of Particle Properties', Phys. Lett. 11B (1982);
G. Goldhaber, 'Review of PEP experiments', talk at the 18th Rencontre de Moriond, La Plagne, France, March 13-19, 1983;
MARK J result from:
B. Adeva et al., Phys. Rev. Lett. 51 (1983) 443.

[6] G.G. Volkov et al., Yad. Fiz. 34 (1981) 419;
Sov. J. Nucl. Phys. 34(2) (1981) 237.

[7] V.V. Abramov et al., Phys. Lett. 78B (1978) 515.

[8] V. Barger et al., Phys. Lett. 116B (1982) 357;
E.L. Berger et al., Phys. Rev. D27 (1983) 1080.

[9] M. Holder et al., Phys. Lett. 70B (1977) 396;
J.G.H. de Groot et al., Phys. Lett. 86B (1979) 103;
T. Trinko et al., Phys. Rev. D23 (1981) 1889;
K. Nishikawa et al., Phys. Rev. Lett. 24 (1981) 1555;
M. Jonker et al., Phys. Lett. 107B (1981) 241.

[10] M.J. Murtagh, Proc. 1979 Int. Symp. on Lepton and Photon Interactions at High Energy, Fermilab. 1979.
H. Fisk and F. Sciulli, Ann. Rev. Nucl. Part. Sci. 32 (1982) 565;
A. Haatuft et al., 21st Int. Conf. on High-Energy Physics, paper nb 747, Paris (1982).

[11] Private communication, R.B. Palmer, BNL.

[12] D.M. Grannan et al., Phys. Rev. D18 (1978) 3150.

[13] J. Ballem et al., Phys. Rev. Lett. 41 (1978) 1207;
N. Craigie, Phys. Reports 47, 1,3 (1978);
J. Stekas et al., Phys. Rev. 47 (1981) 24;
B. Haber et al., Phys. Rev. D22 (1980) 2107;
R. Stroynowski et al., Phys. Lett. 97B (1980) 315;
K. Bunell et. al., Phys. Rev. Lett. 40 (1978) 136;
R. Stroynowski, Phys. Rep. 71 (1981) 1.

[14] J.D. Björken and H. Weisberg, Phys. Rev. D13 (1976) 1405.

[15] H. Fischer and W. Geist, Z. Phys. C 19 (1983) 159.

[16] F.E. Paige and S.D. Protopropescu, ISAJET: A Monte Carlo Generator for pp and $p\bar{p}$ interactions, BNL 297 77 (1980).

[17] S. Hancock et al., Energy Loss and Energy-Straggling of Protons and Pions in the Momentum Range 0.7 to 115 GeV/c; CERN-EP/83-76.

[18] A. Bodek et al., Phys. Lett. 113B (1982) 77.

[19] B. Hyams et al., Nucl. Instr. Meth. 205 (1983) 99.

[20] S. Bobkov et al., Drift precision imager, CERN-EP/83-81.

[21] R.A. Boie et al., IEEE Trans. Nucl. Sci. NS 28 (1981) 603.

[22] D. Bettoni et al., International Europhysics Conference on High Energy Physics, Brighton, UK, (1983).

[23] C.W. Fabjan et al., Optimization of cluster-counting transition radiation detectors, CERN-EP/83-45, to be published in Nucl. Instr. Meth.

[24] J. Badier et al., Nucl. Instr. Meth. 175 (1980) 319.

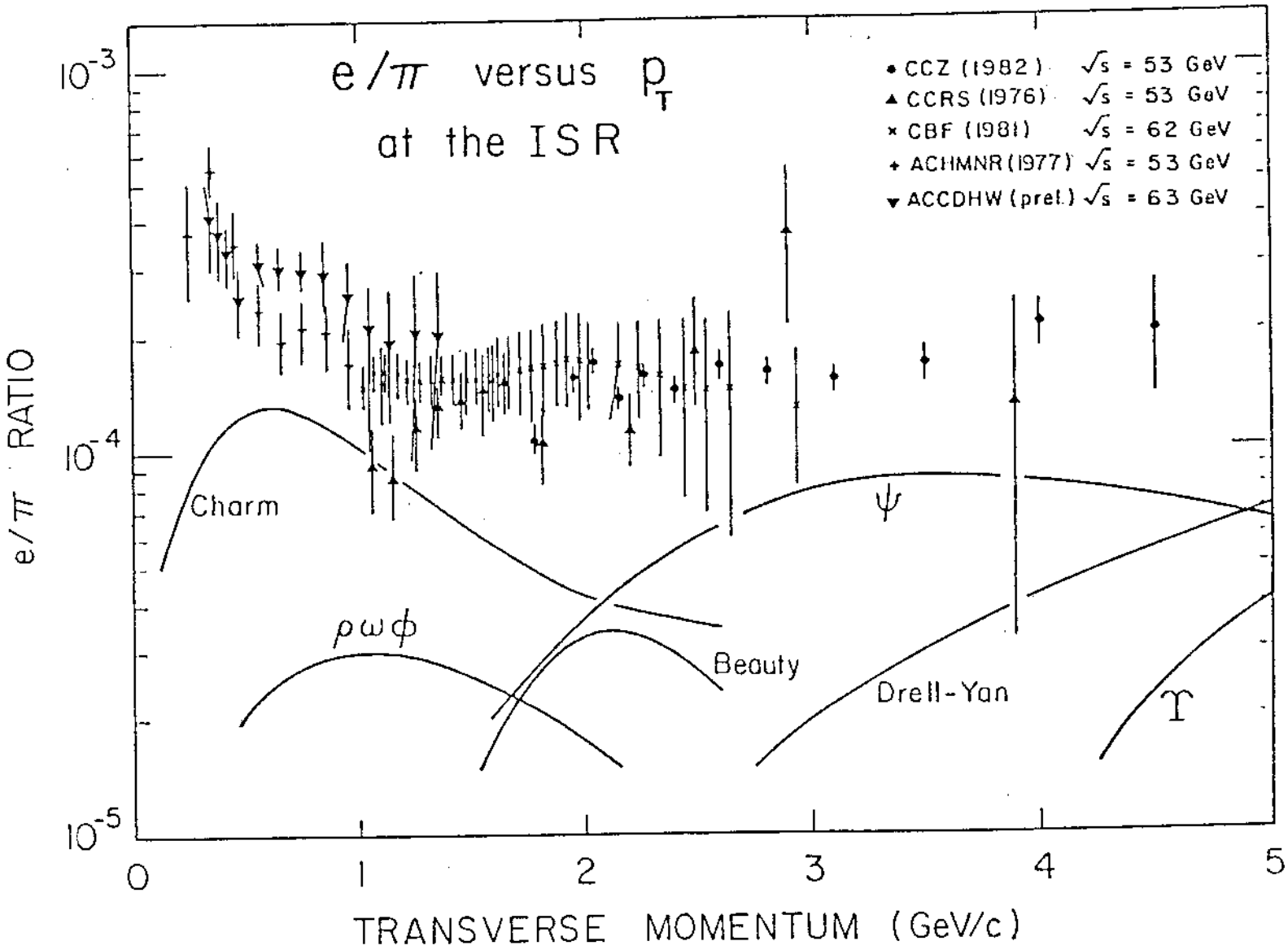
e/π versus p_T
at the ISR
• CCZ (1982) √s = 53 GeV
▲ CCRS (1976) √s = 53 GeV
× CBF (1981) √s = 62 GeV
+ ACHMNR (1977) √s = 53 GeV
▼ ACCDHW (prel.) √s = 63 GeV
e/π RATIO
10^{-3}
10^{-4}
10^{-5}
Charm
ρωφ
Beauty
ψ
Drell-Yan
Υ
0
1
2
3
4
5
TRANSVERSE MOMENTUM (GeV/c)

Fig. 1

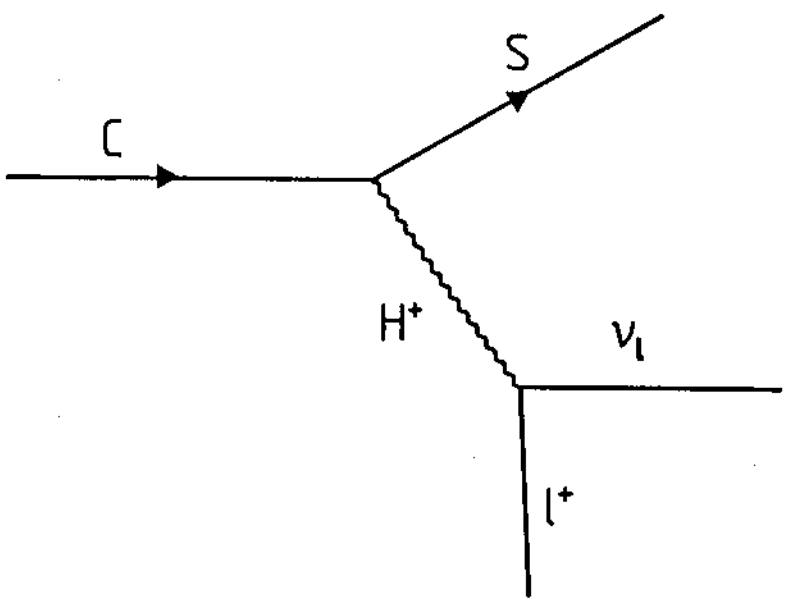

Fig. 2

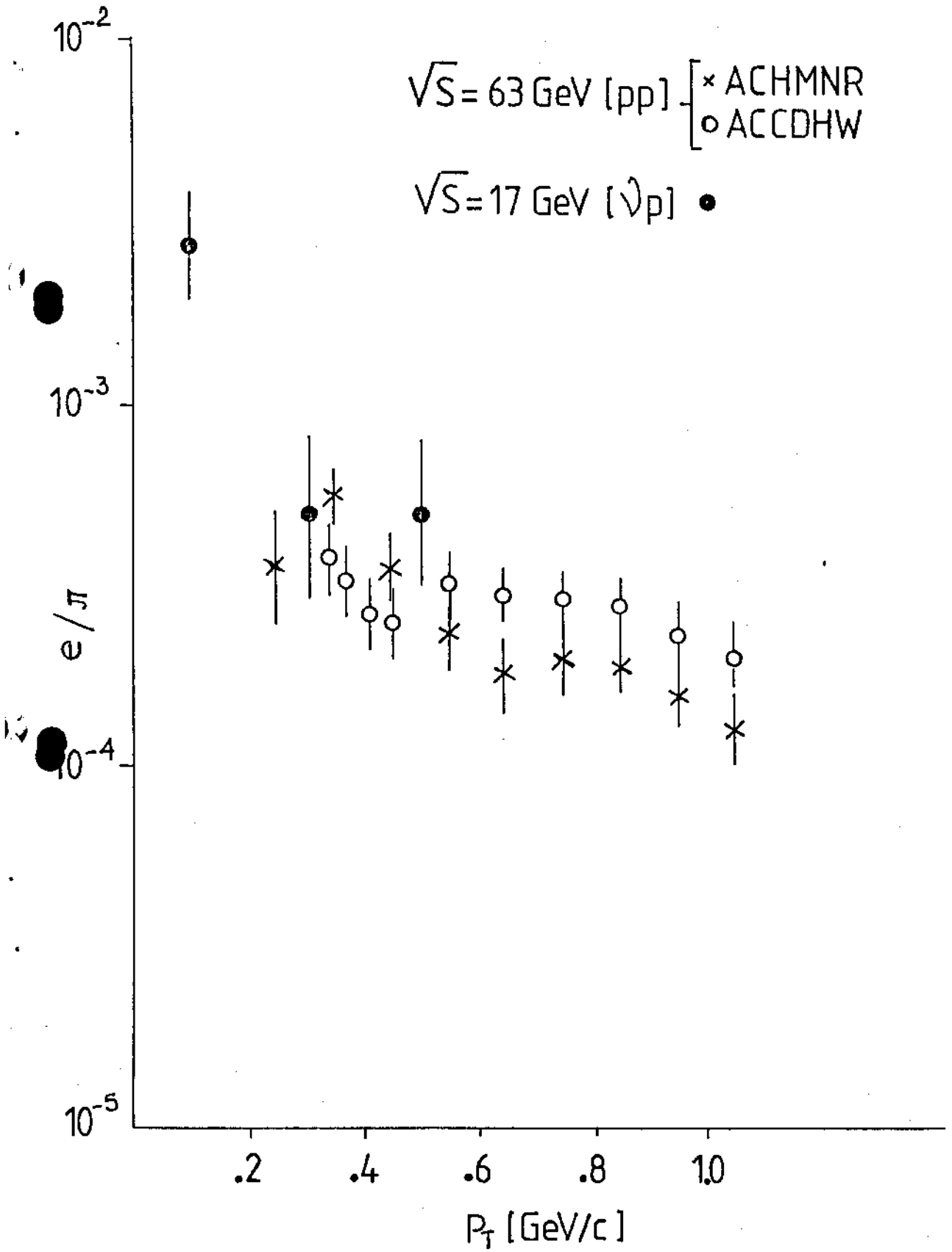
10^{-2}
10^{-3}
10^{-4}
10^{-5}
e/π
$\sqrt{S}$ = 63 GeV [pp]
× ACHMNR
○ ACCDHW
$\sqrt{S}$ = 17 GeV [ν̄p] ●
.2
.4
.6
.8
1.0
P_T [GeV/c]

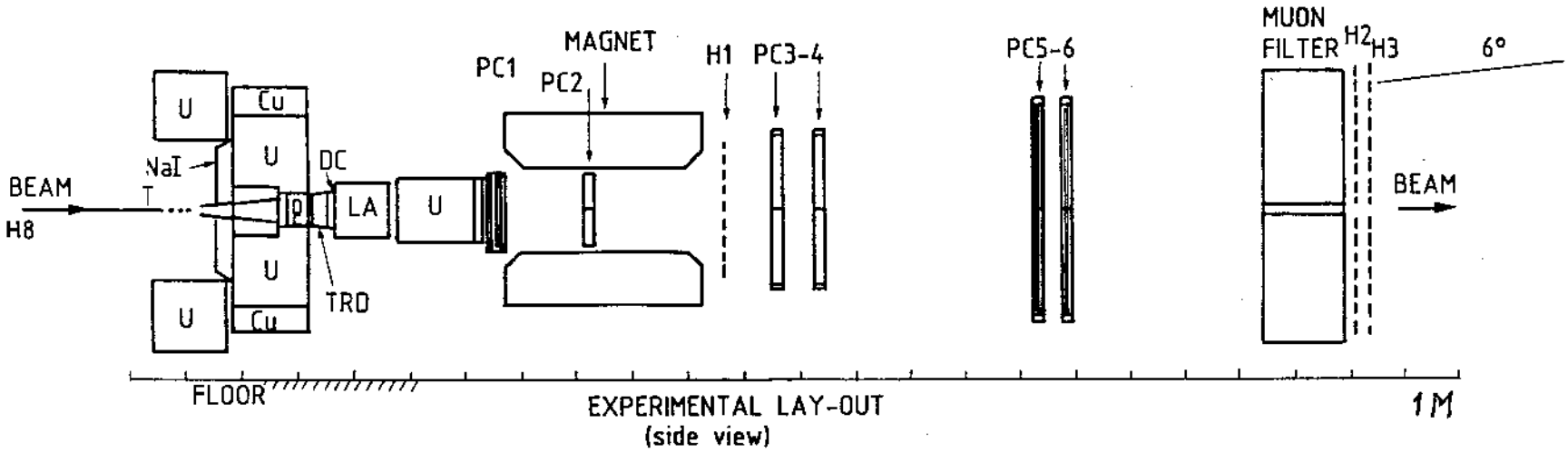
MUON
FILTER
H2
H3
6°
MAGNET
PC1
PC2
H1
PC3-4
PC5-6
U
Cu
U
NaI
DC
BEAM
H8
P
LA
U
U
Cu
TRD
BEAM
FLOOR
EXPERIMENTAL LAY-OUT
(side view)
1M

Fig. 4a

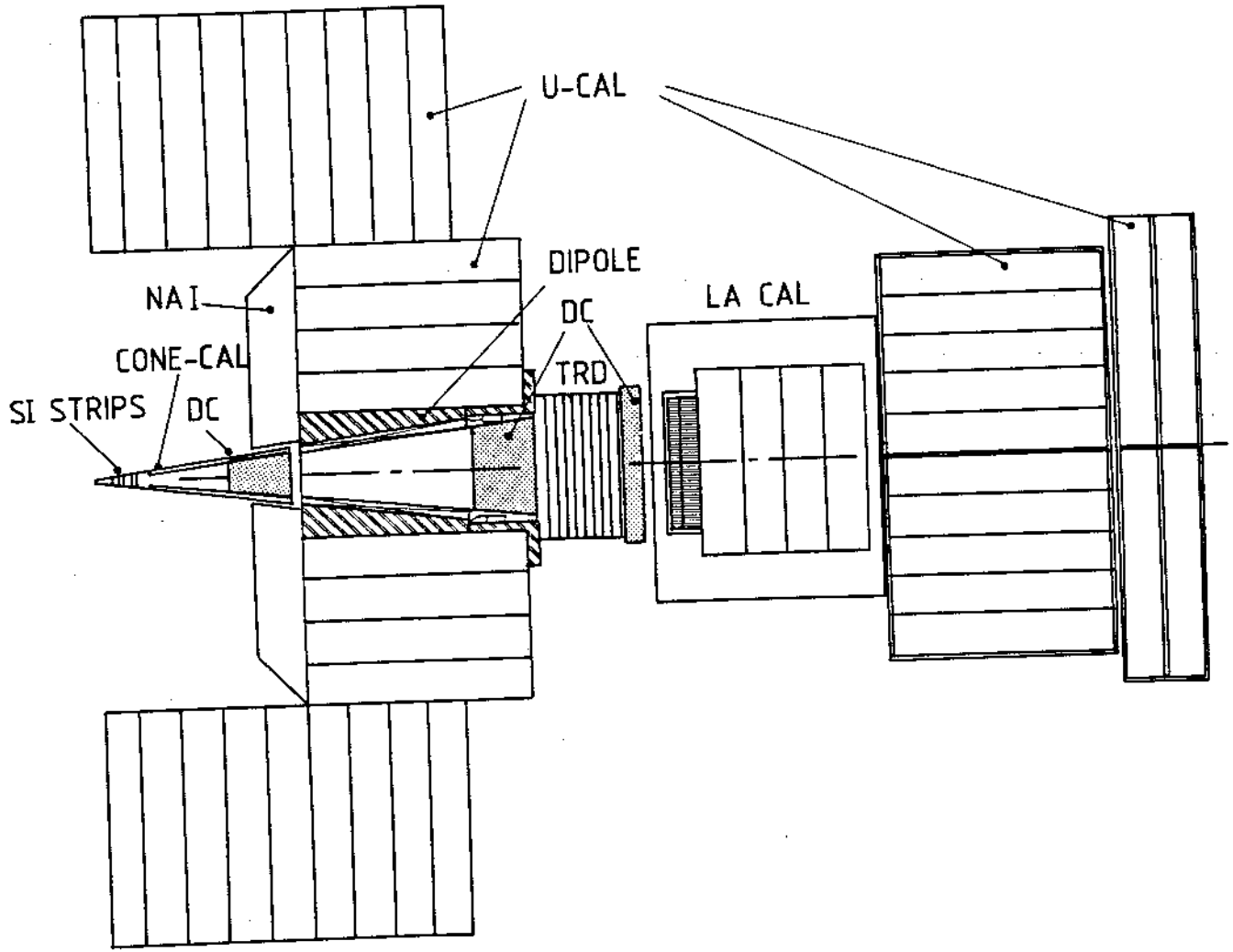

Fig. 4b

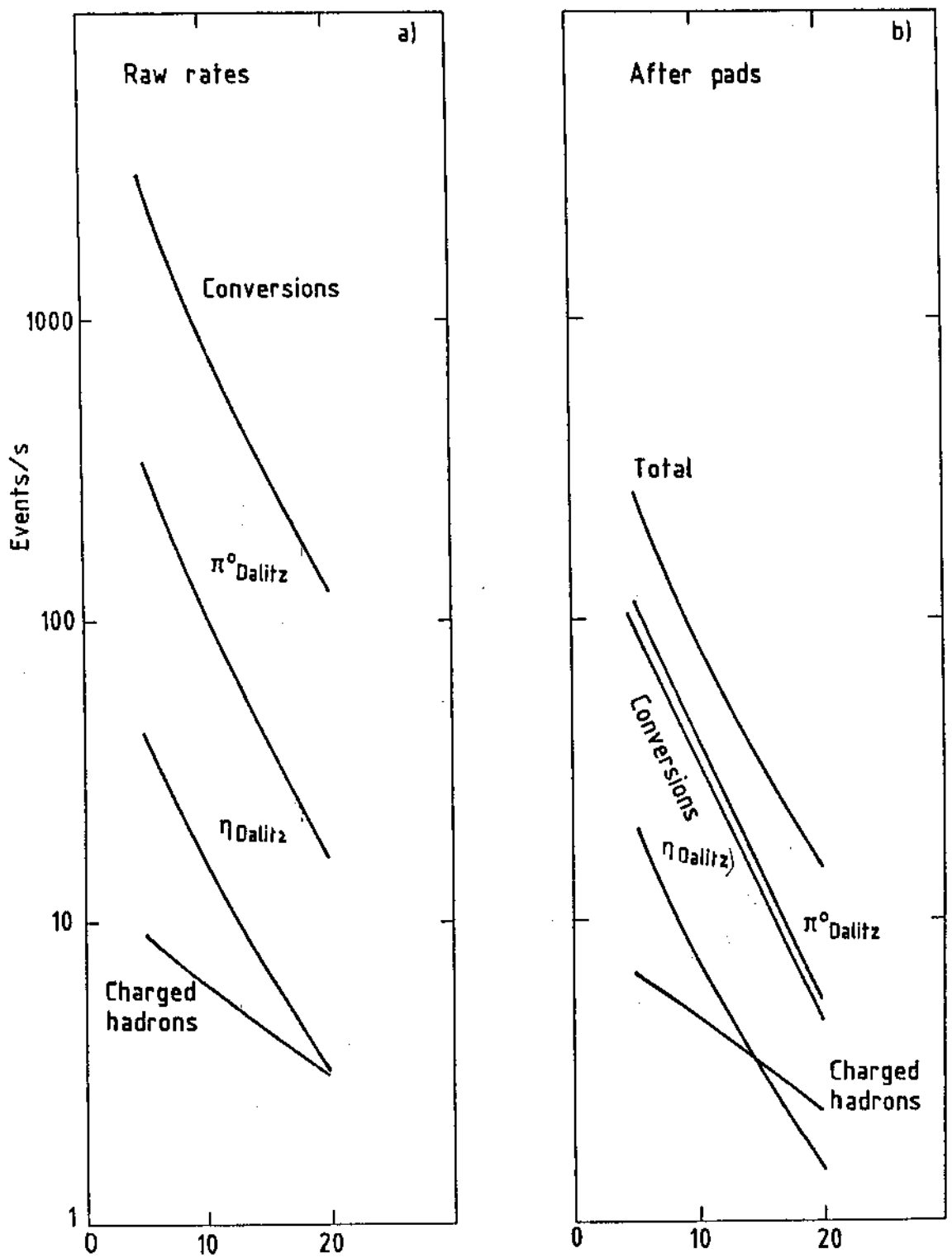
a)
Raw rates
Conversions
π^0_{Dalitz}
η_{Dalitz}
Charged hadrons
Events/s
1000
100
10
1
0
10
20
b)
After pads
Total
Conversions
η_{Dalitz}
π^0_{Dalitz}
Charged hadrons
0
10
20
Threshold energy of the electrons (GeV)

Fig. 5a

Fig. 5b

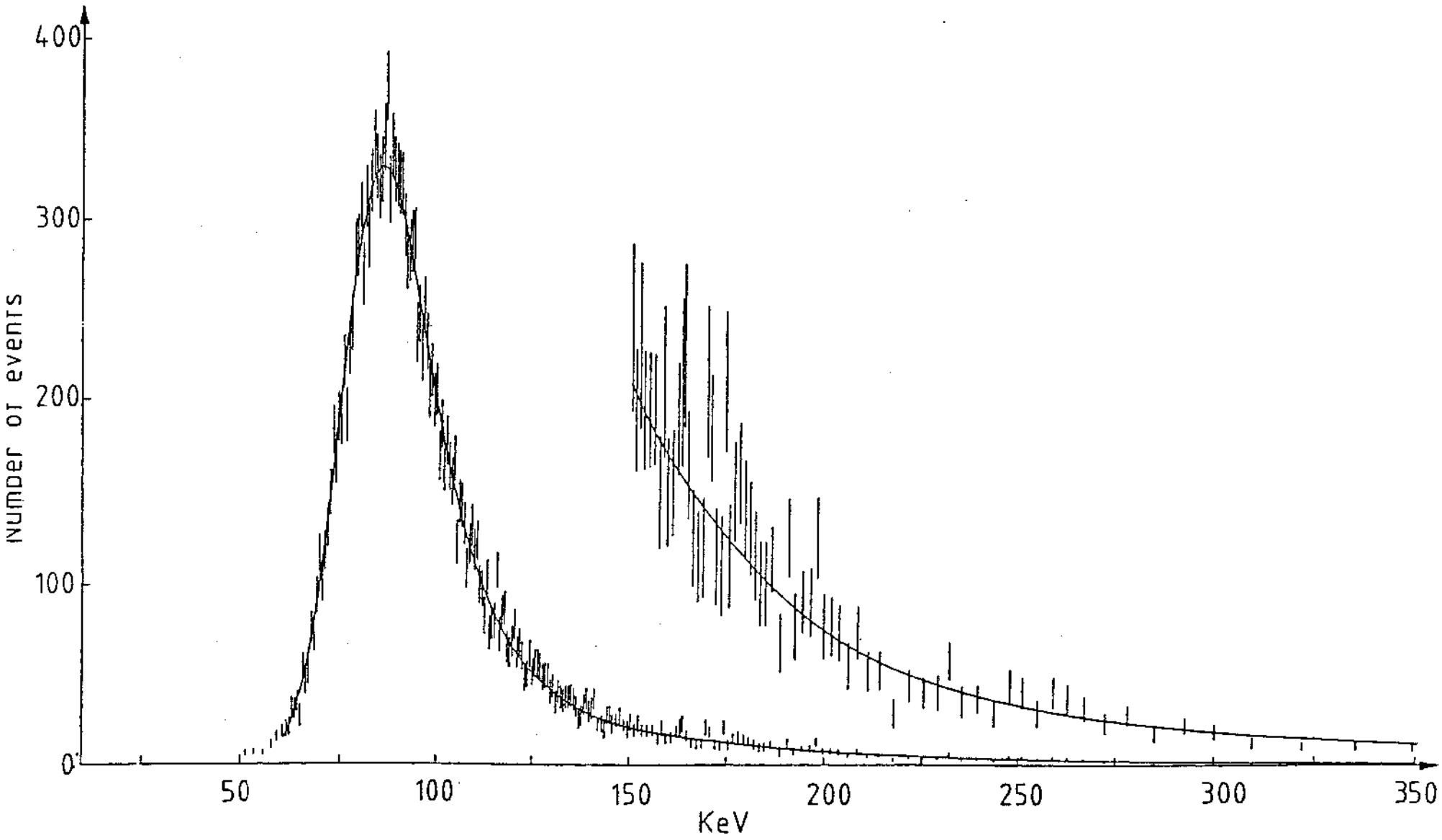
400
300
200
100
0
Number of events
50
100
150
200
250
300
350
KeV

Fig. 6

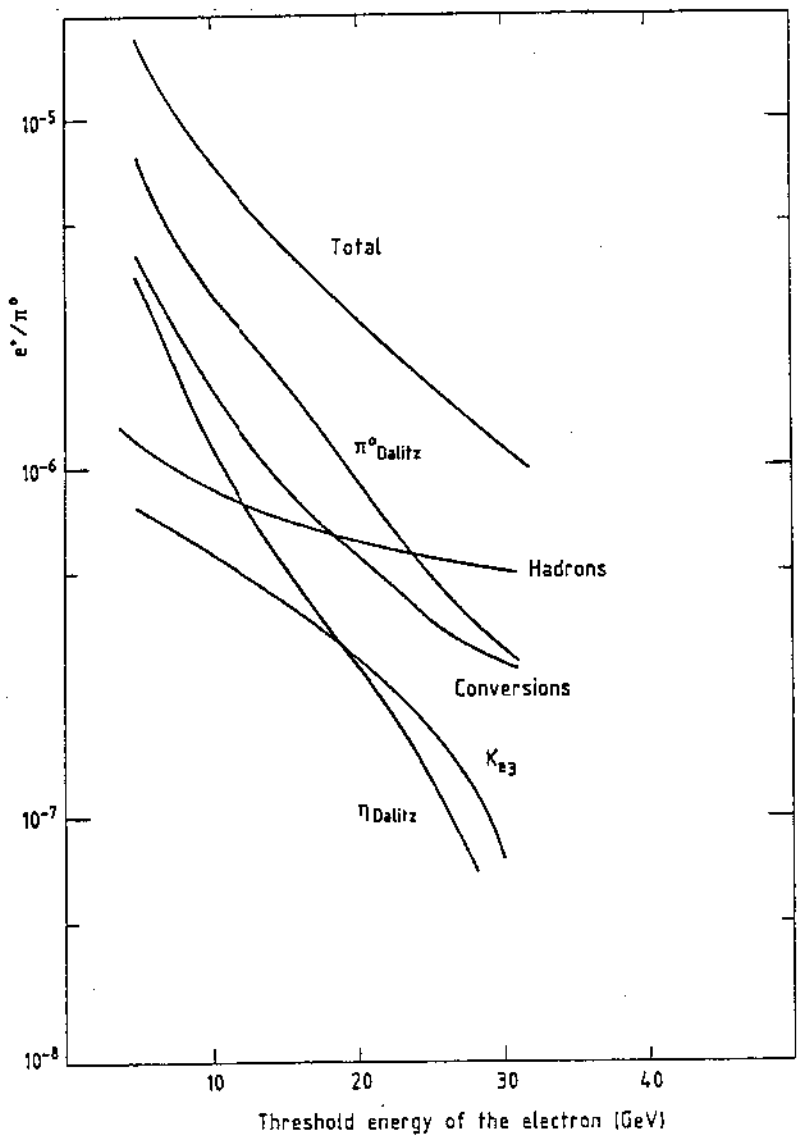
10^{-5}
10^{-6}
10^{-7}
10^{-8}
e^+/π^0
Total
π^0_{Dalitz}
Hadrons
Conversions
K_{e3}
η_{Dalitz}
10
20
30
40
Threshold energy of the electron (GeV)

Fig. 7

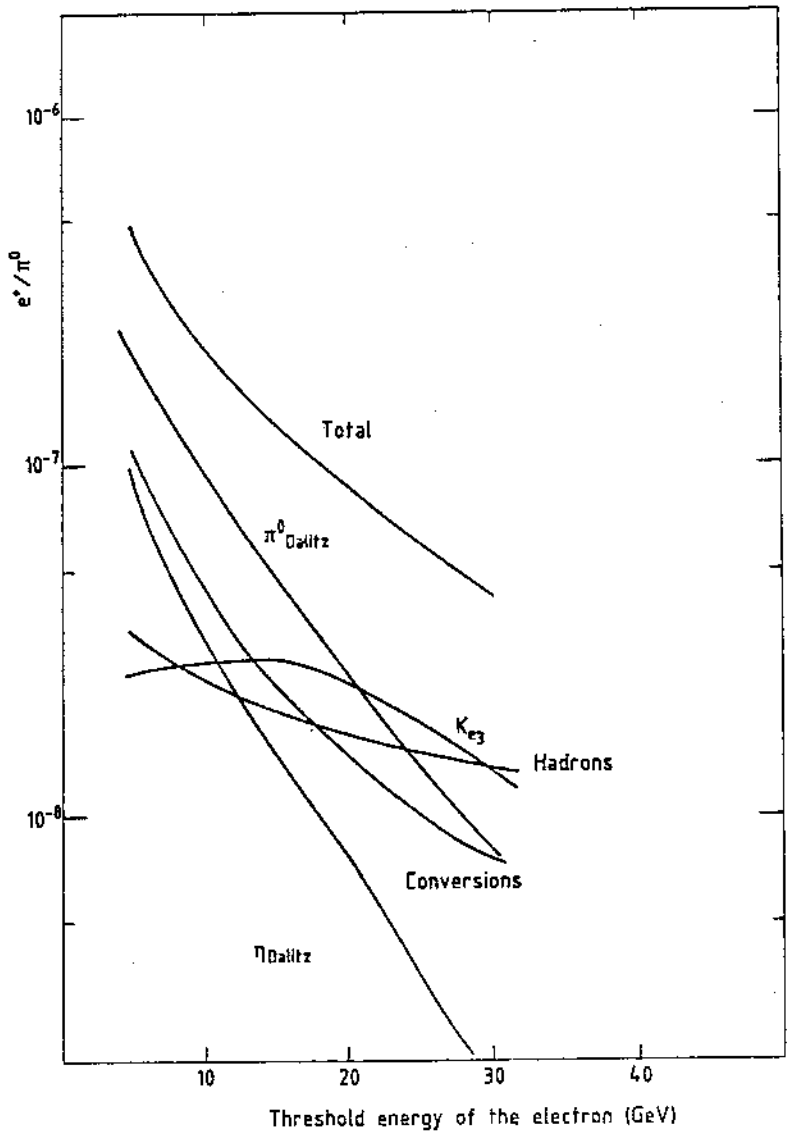
10^{-6}
10^{-7}
10^{-8}
e^+/π^0
Total
π^0_{Dalitz}
K_{e3}
Hadrons
Conversions
η_{Dalitz}
10
20
30
40
Threshold energy of the electron (GeV)

Fig. 8

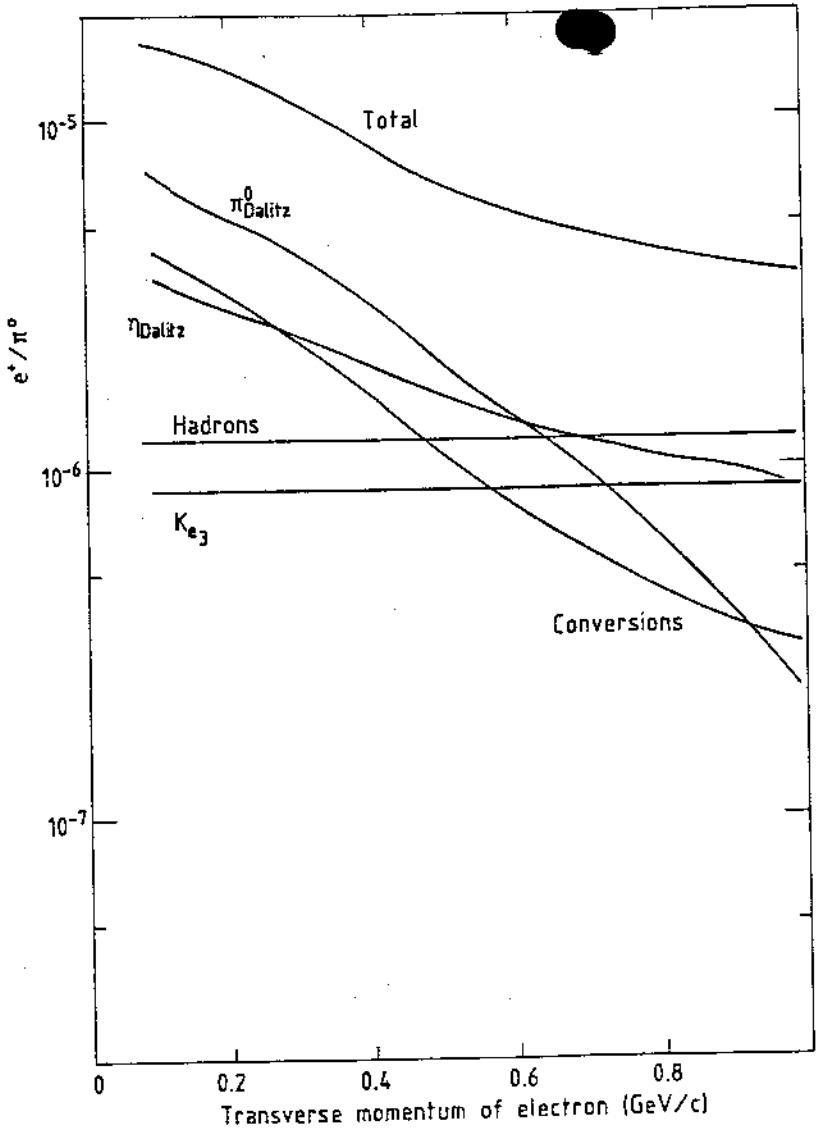
Total
π^0_{Dalitz}
η_{Dalitz}
Hadrons
K_{e_3}
Conversions
e^+/π^0
10^{-5}
10^{-6}
10^{-7}
0
0.2
0.4
0.6
0.8
Transverse momentum of electron (GeV/c)

Fig. 9

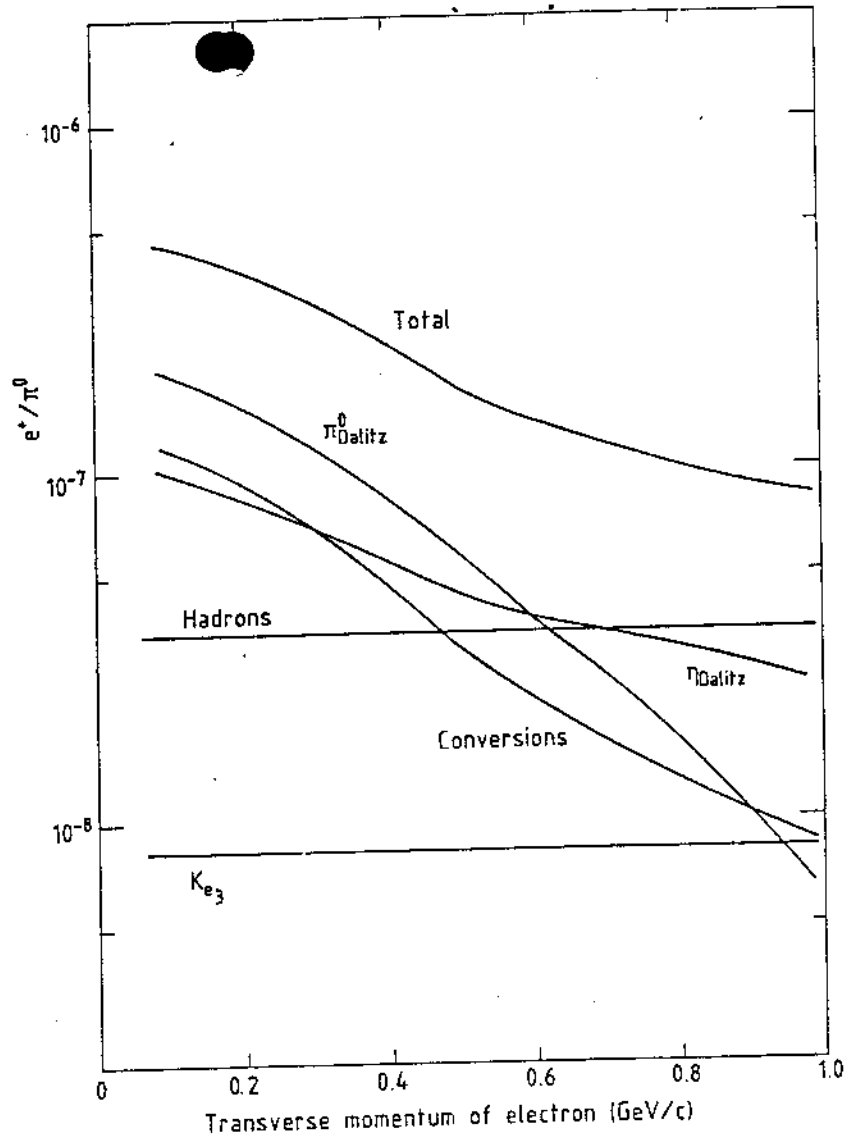
Total
π^0_{Dalitz}
Hadrons
η_{Dalitz}
Conversions
K_{e_3}
e^+/π^0
10^{-6}
10^{-7}
10^{-8}
0
0.2
0.4
0.6
0.8
1.0
Transverse momentum of electron (GeV/c)

Fig. 10

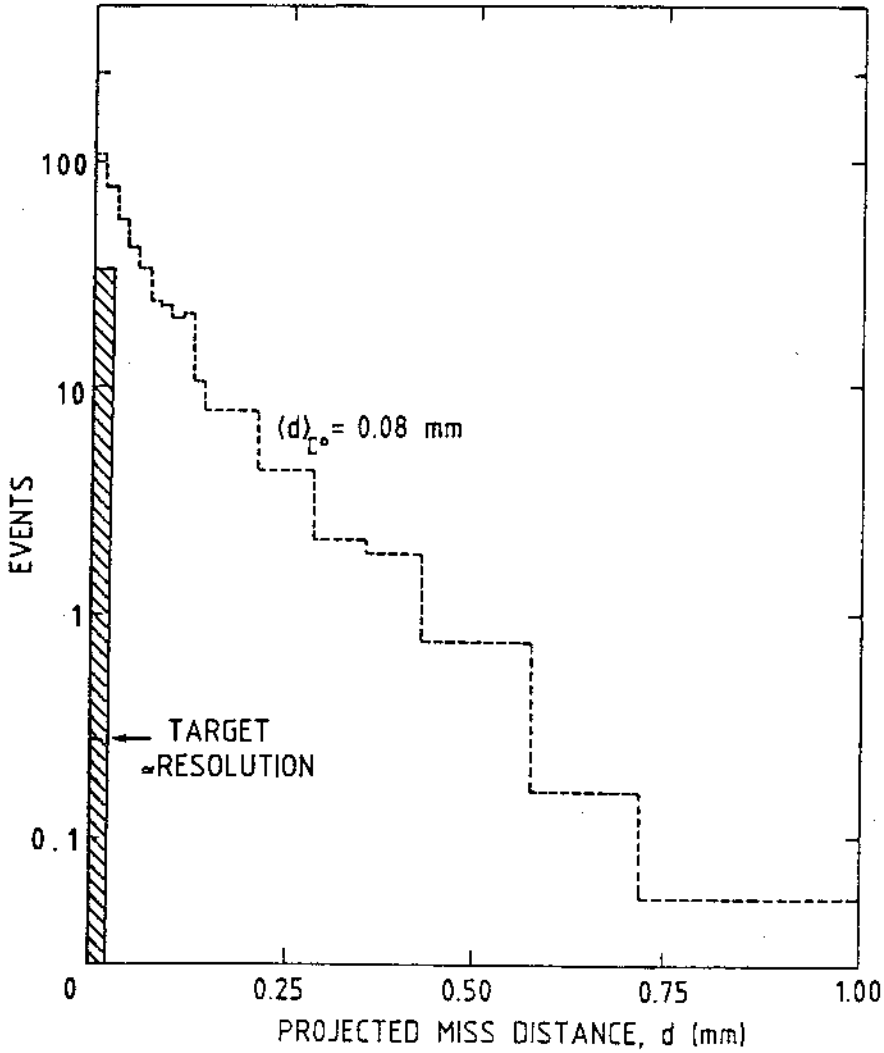

Fig. 11a

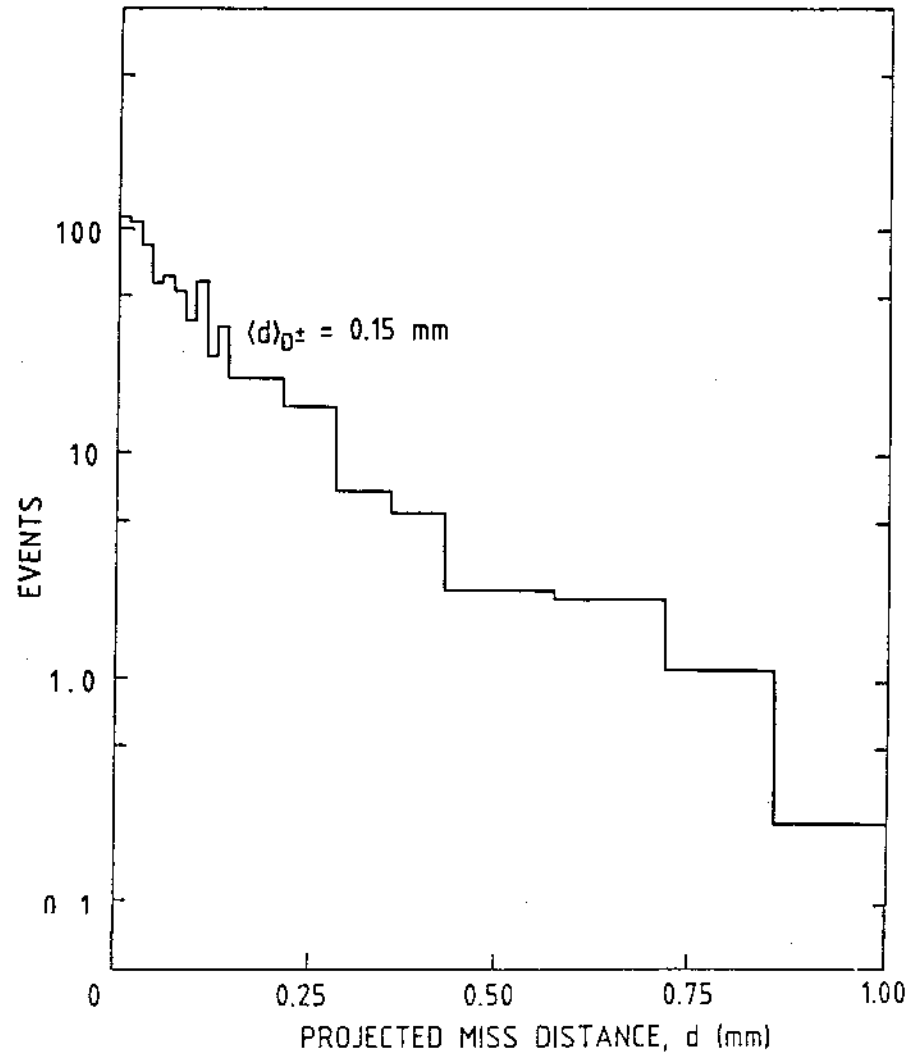

Fig. 11b

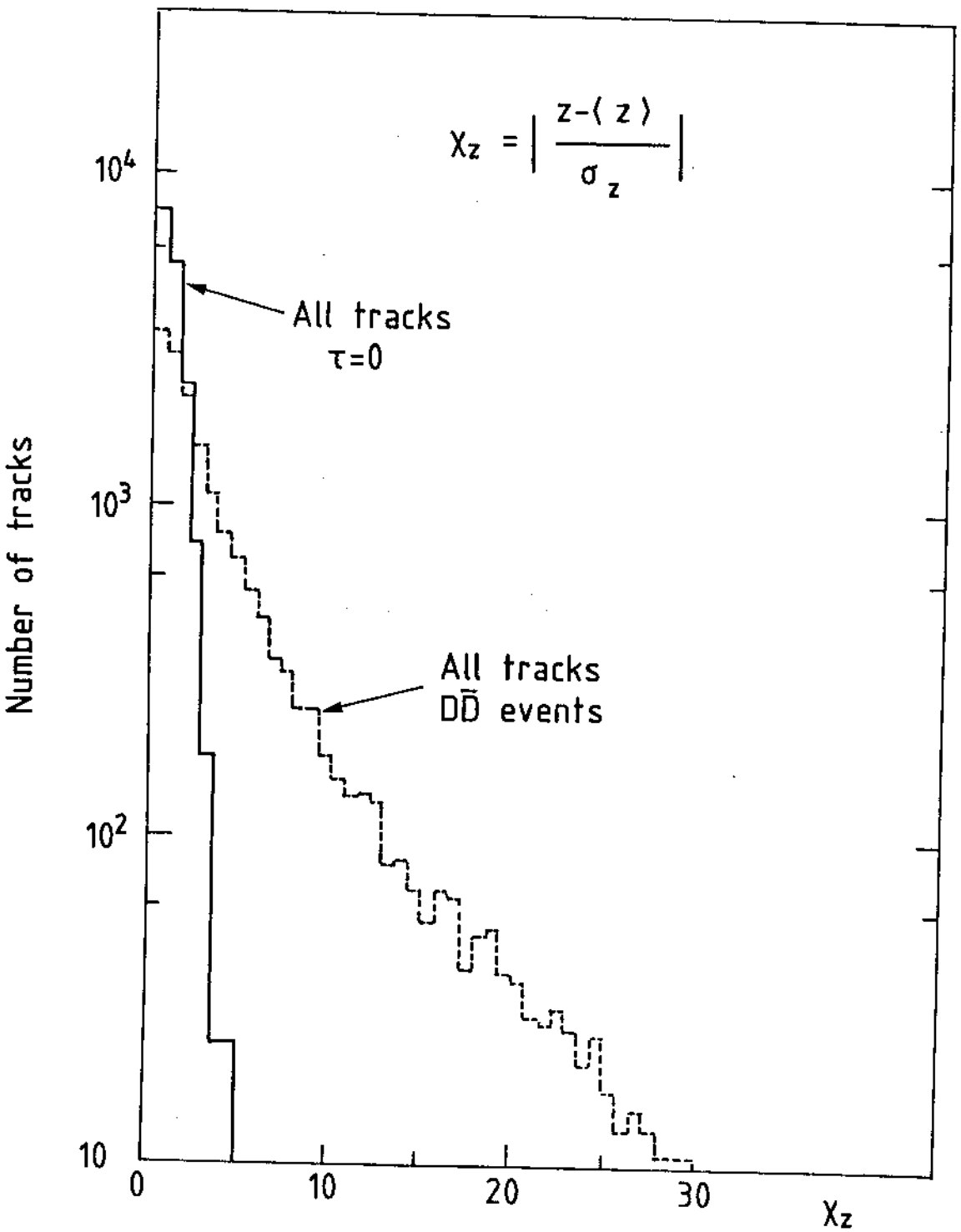
$X_z = \left| \frac{z-\langle z \rangle}{\sigma_z} \right|$
All tracks
τ=0
All tracks
DD̄ events
Number of tracks
10⁴
10³
10²
10
0
10
20
30
X_z

Fig. 12

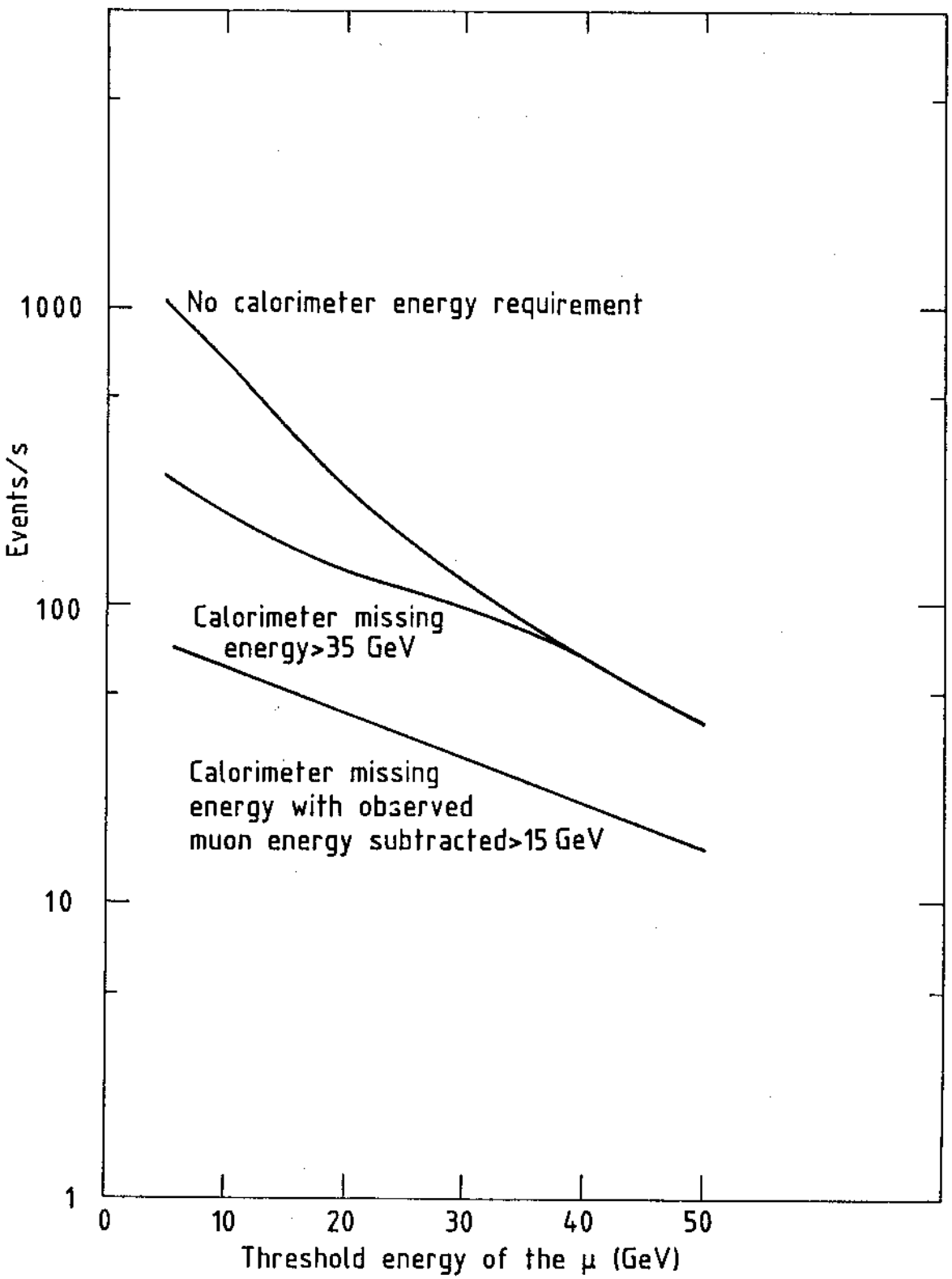
No calorimeter energy requirement
Calorimeter missing energy>35 GeV
Calorimeter missing energy with observed muon energy subtracted>15 GeV
Events/s
1000
100
10
1
0
10
20
30
40
50
Threshold energy of the μ (GeV)

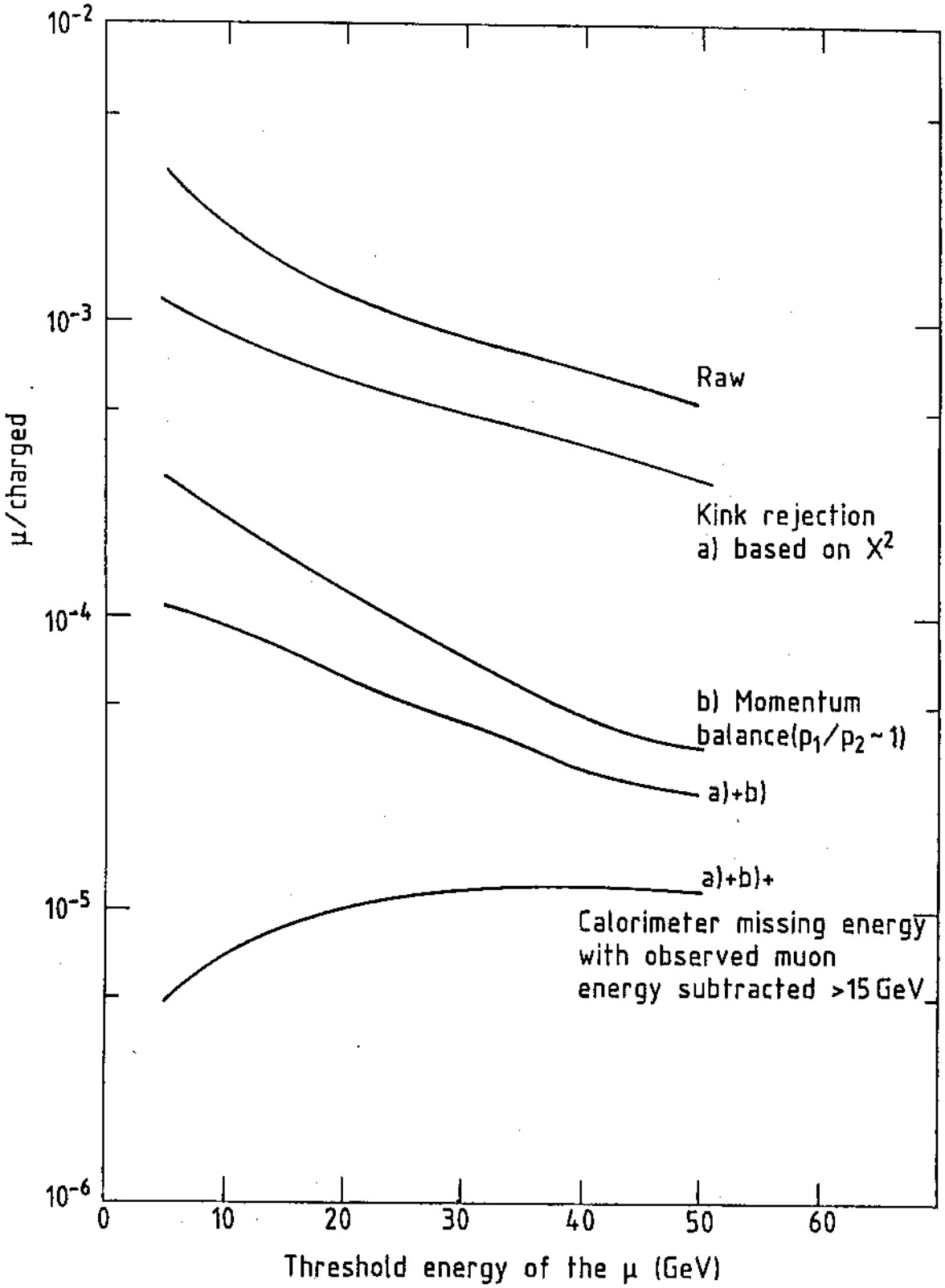
10^{-2}
10^{-3}
10^{-4}
10^{-5}
10^{-6}
μ/charged
Raw
Kink rejection
a) based on X^2
b) Momentum
balance($p_1/p_2 \sim 1$)
a)+b)
a)+b)+
Calorimeter missing energy
with observed muon
energy subtracted >15 GeV
0
10
20
30
40
50
60
Threshold energy of the μ (GeV)

Fig. 14

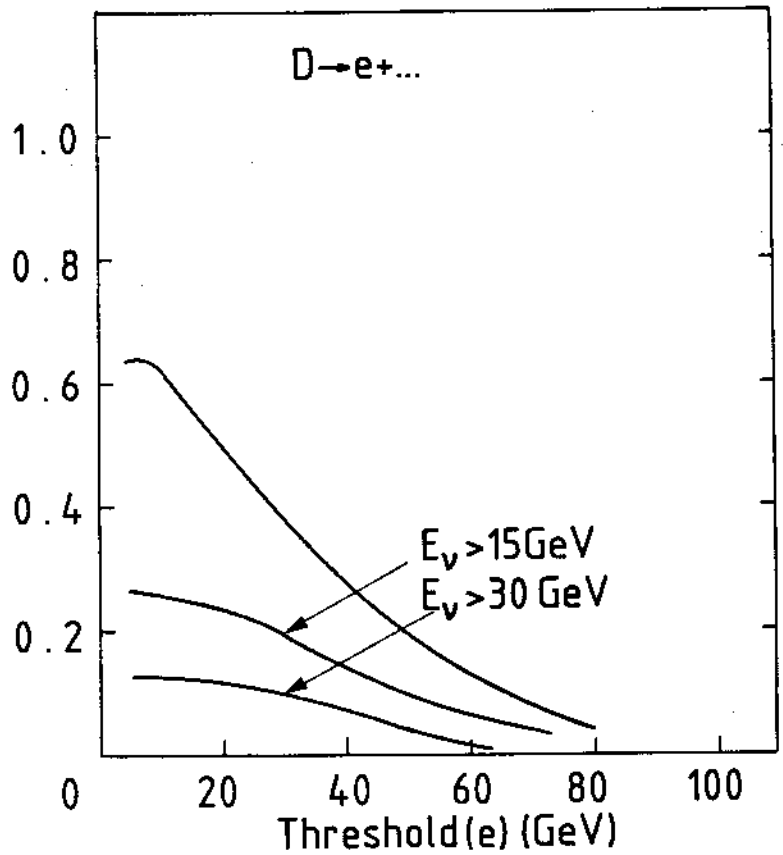

Fig. 15a

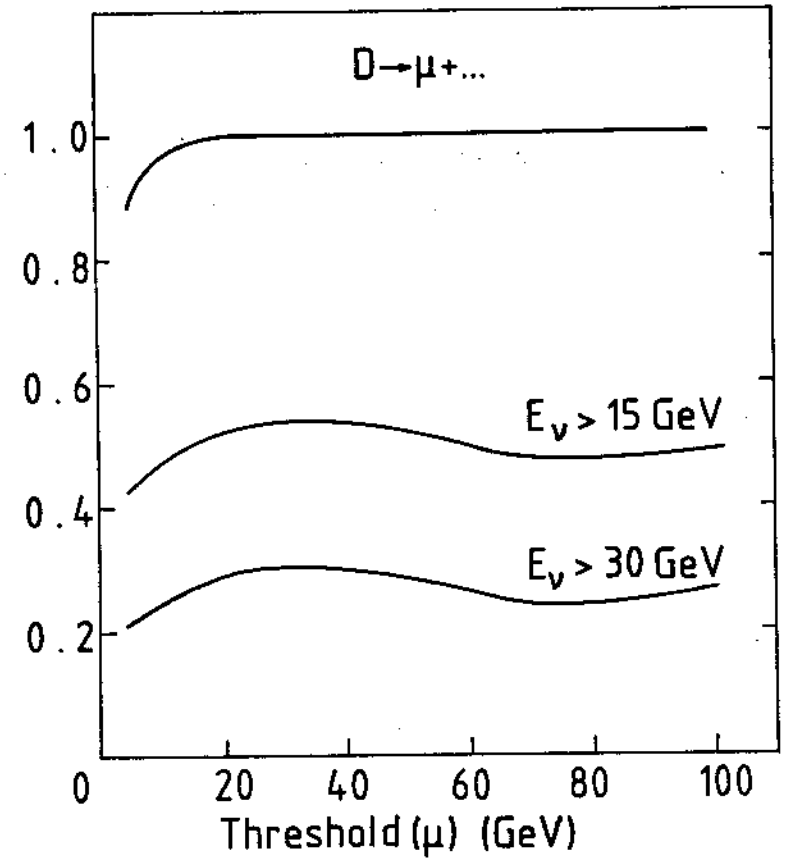

Fig. 15b

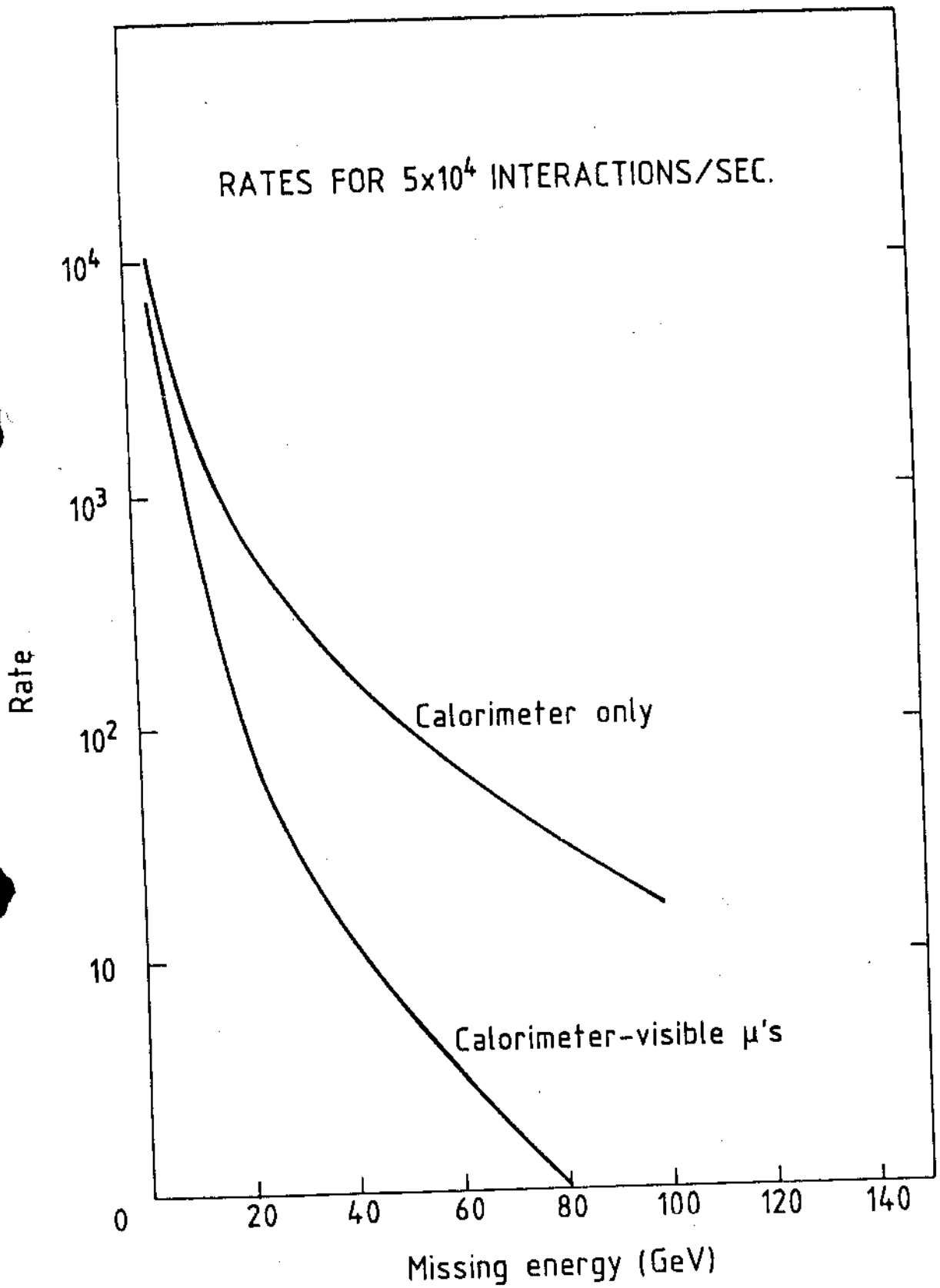
RATES FOR 5x10⁴ INTERACTIONS/SEC.
Rate
10⁴
10³
10²
10
0
Calorimeter only
Calorimeter-visible μ's
20
40
60
80
100
120
140
Missing energy (GeV)

Fig. 16

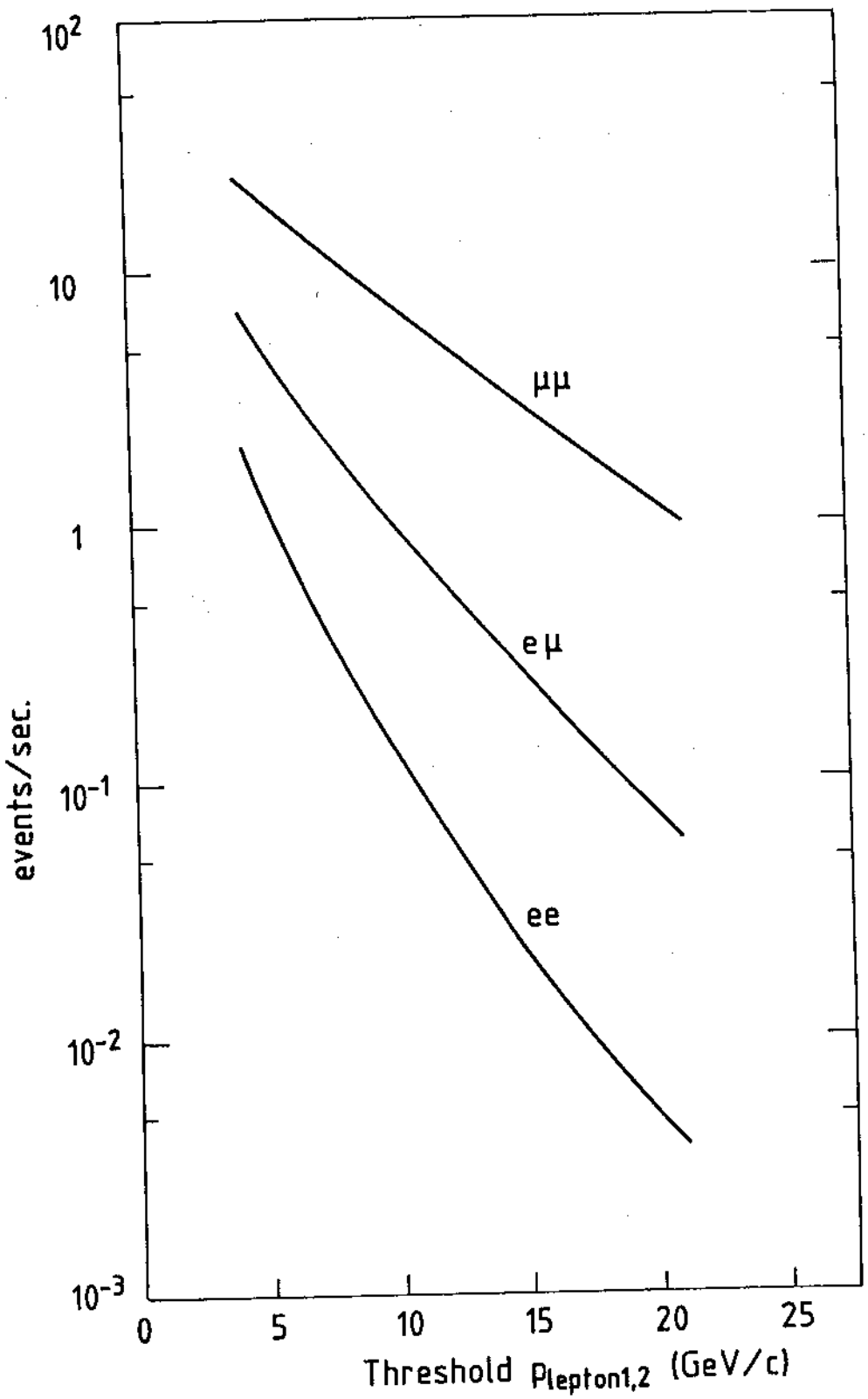
10^2
10
1
10^{-1}
10^{-2}
10^{-3}
events/sec.
μμ
eμ
ee
0
5
10
15
20
25
Threshold $p_{lepton1,2}$ (GeV/c)

Fig. 17

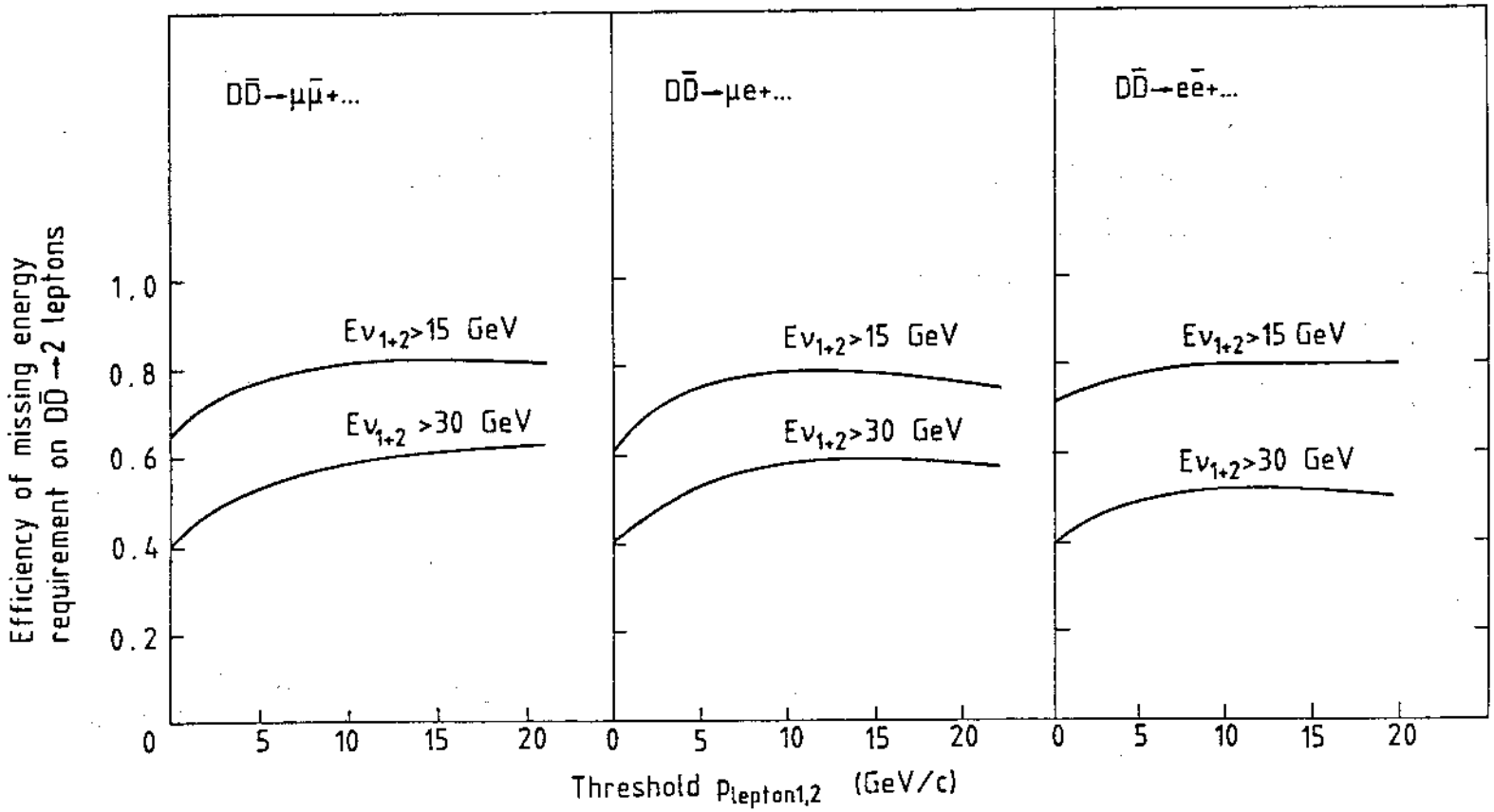
DD̄→μμ̄+...
DD̄→μe+...
DD̄→ee+...
Eν1+2>15 GeV
Eν1+2 >30 GeV
Eν1+2>15 GeV
Eν1+2>30 GeV
Eν1+2>15 GeV
Eν1+2>30 GeV
Efficiency of missing energy requirement on DD̄→2 leptons
1.0
0.8
0.6
0.4
0.2
0
5
10
15
20
Threshold Plepton1,2 (GeV/c)

Fig. 18

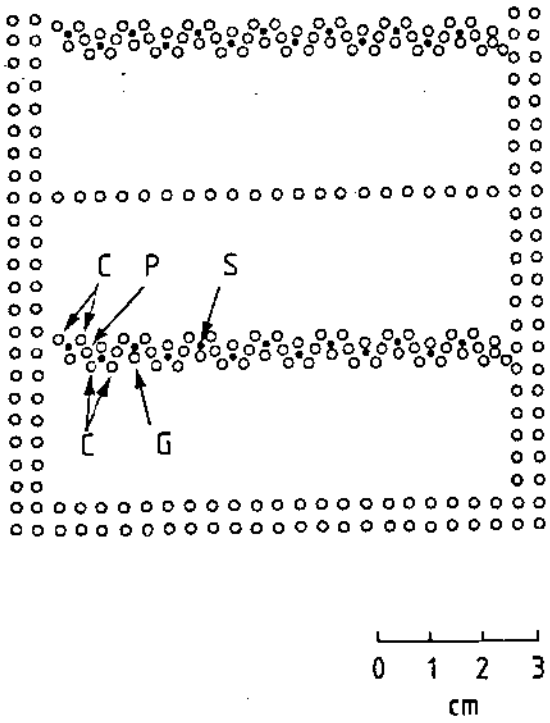
C
P
S
C
G
0
1
2
3
cm

Fig. 19

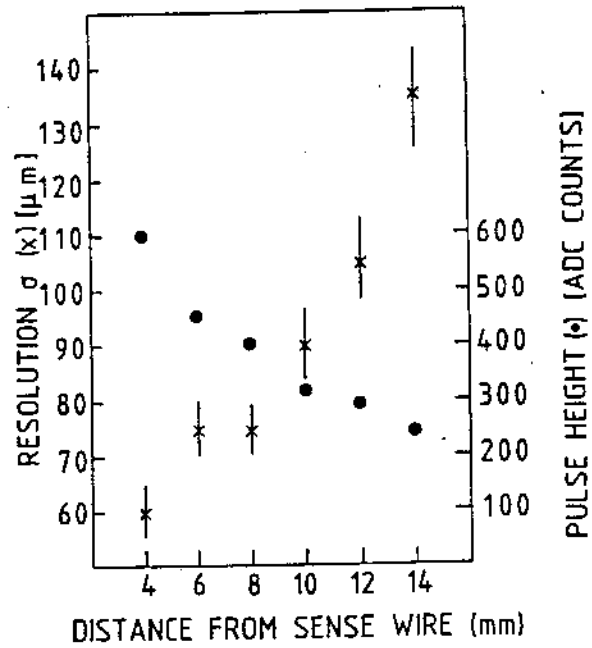
RESOLUTION σ (x) [μm]
PULSE HEIGHT (•) [ADC COUNTS]
DISTANCE FROM SENSE WIRE (mm)
140
130
120
110
100
90
80
70
60
600
500
400
300
200
100
4
6
8
10
12
14

Fig. 20

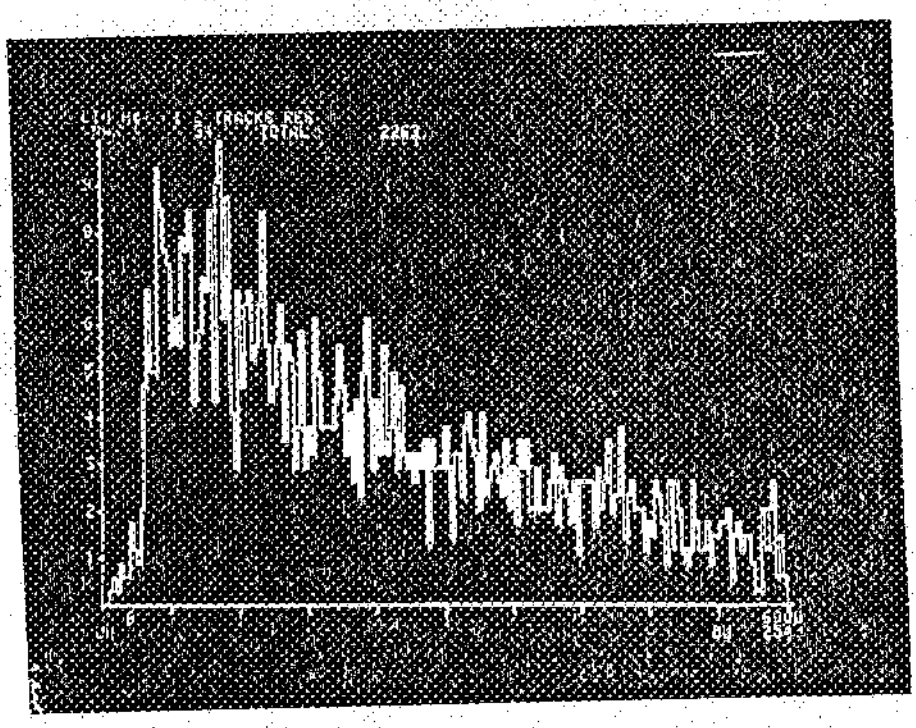

Fig. 21